

Modeling and dynamics of axisymmetric thin liquid film flow along a conical surface

Longmin Tang¹ and Guangzhao Zhou^{1, 2†}

¹School of Engineering Science, University of Chinese Academy of Sciences, Beijing 101408, China

²State Key Laboratory of Nonlinear Mechanics, IMECH & UCAS, Beijing 100190, China

(Received xx; revised xx; accepted xx)

This study focuses on the modeling and dynamics of gravity-driven, axisymmetric thin liquid film flow along a conical surface. Spatial linear stability analysis is performed on the basis of a Benney-type equation derived for the present configuration. In particular, streamwise curvature of the free surface is found to exert a crucial influence on the stability threshold. For simulations of surface waves, a second-order low-dimensional model is developed under the long-wave assumption, achieving accuracy comparable to direct numerical simulations at far lower cost. With this model, the characteristics of both linear and nonlinear waves are examined. A key difference from the flow over a flat plate is the dependence of wave dynamics on radial distance from the cone apex. At relatively high flow rates, a transition from solitary to sinusoidal waves is observed, with the transition position correlating closely with the linear stability threshold. Within the parameter range investigated, quantitative results of the conical film flow are almost identical to those in the flat-plate case when local parameters are substituted, indicating that inertial effects of the conical geometry are negligible. The models and findings presented in this paper may aid the design and optimization of industrial processes such as film coating and liquid-film-based heat and mass transfer on conical surfaces.

1. Introduction

Thin liquid film flows along solid surfaces are ubiquitous in daily life. They are also widely employed in industrial heat and mass transfer applications because of their large surface-to-volume ratios. Examples include gas absorption (Hu *et al.* 2014), desalination (Dai *et al.* 2022), and distillation (Valluri *et al.* 2005). Since the pioneering experimental work of Kapitza (1948) and Kapitza & Kapitza (1949), the study of liquid film flow has remained an active area of both fundamental and applied research, attracting sustained attention for decades.

The physical understanding and mathematical description of gravity-driven liquid film flow over a flat plate have been extensively studied (Chang 1994; Chang & Demekhin 2002; Weinstein & Ruschak 2004; Craster & Matar 2009; Kalliadasis *et al.* 2012; Bandi *et al.* 2018). For a given volumetric flow rate per unit width, \tilde{Q}_{2D} , the thickness of an undisturbed film, known as the Nusselt film thickness (Nusselt 1916), is

$$\tilde{h}_{N2D} = \left(\frac{3\nu\tilde{Q}_{2D}}{g \sin \tilde{\varphi}} \right)^{1/3}, \quad (1.1)$$

where ν is the kinematic viscosity of the liquid, g is the gravitational acceleration, and $\tilde{\varphi}$ is the plate's inclination angle relative to the horizontal plane. Linear stability analysis shows

† Email address for correspondence: zgz@ucas.ac.cn

that when the Reynolds number, defined as

$$Re_{2D} = \frac{\tilde{Q}_{2D}}{\nu}, \quad (1.2)$$

exceeds $5 \cot(\tilde{\varphi})/6$ (Benjamin 1957; Yih 1963), the film becomes unstable to low-wavenumber disturbances. The cut-off wavenumber \tilde{k}_{c2D} below which the flow is unstable satisfies (see, e.g., Kalliadasis *et al.* 2012, p. 196)

$$\tilde{k}_{c2D} \tilde{h}_{N2D} = \frac{1}{\sqrt{We}} \left(\frac{6}{5} Re_{2D} - \cot \tilde{\varphi} \right)^{1/2}, \quad (1.3)$$

where the Weber number defined in their context is $We = \sigma/(\rho g \tilde{h}_{N2D}^2 \sin \tilde{\varphi})$, which is essentially an inverse Bond number. ρ and σ are density and surface tension coefficient of the liquid, respectively. Eq. (1.3) shows that the linear stability is influenced by the combined effects of inertia, viscosity, and surface tension force. Specifically, the surface tension plays a role of stabilization.

When the flow is unstable, small-amplitude disturbances on the free surface first grow according to linear theory and eventually saturate as finite-amplitude nonlinear waves. If the dynamics is dominated by a single wavelength—e.g., when a monochromatic disturbance is imposed at the inlet—the free-surface profile is spatially periodic. The resulting shape depends on the wavelength $\tilde{\lambda}$ (Liu & Gollub 1994; Malamataris *et al.* 2002): short waves are nearly sinusoidal, whereas long waves form solitary humps preceded by small capillary ripples within each wave unit (Joo *et al.* 1991; Chang 1994; Chang & Demekhin 2002; Rohlfs & Scheid 2015; Zhou & Prosperetti 2020a). Considering the critical role of the wavy structures in heat and mass transfer (Miyara 1999; Sisoev *et al.* 2005; Charogiannis & Markides 2019; Dietze 2019; Zhou & Prosperetti 2020b), much effort has been devoted to examine the dynamics of these surface waves both experimentally (e.g., Alekseenko *et al.* 1985; Liu *et al.* 1993; Liu & Gollub 1994; Nosoko *et al.* 1996; Meza & Balakotaiah 2008; Dietze *et al.* 2009; Kofman *et al.* 2014) and numerically (e.g., Malamataris *et al.* 2002; Mudunuri & Balakotaiah 2006; Dietze *et al.* 2014; Chakraborty *et al.* 2014; Denner *et al.* 2016).

In numerical simulations, since the streamwise dimension of the liquid film is usually much larger than the film thickness, with a moderate cell aspect ratio, a very large total number of mesh cells is required, making the computation expensive. Two main strategies have been used to reduce the cost. The first exploits periodicity: a single wave unit is simulated with periodic boundary conditions at both ends of it (see, e.g., Salamon *et al.* 1994; Ramaswamy *et al.* 1996; Aktershev 2010). The second relies on the separation of streamwise and cross-stream scales, which allows development of a variety of low-dimensional models (see, e.g., Nguyen & Balakotaiah 2000; Ruyer-Quil & Manneville 2000; Scheid *et al.* 2006; Mudunuri & Balakotaiah 2006; Samanta 2023). In derivation of these models, a certain type of integration with respect to the cross-stream coordinate is performed through the film thickness. Therefore, for two-dimensional liquid films, the flow field is explicitly dependent on the streamwise coordinate only. The computational efficiency is significantly improved compared with direct numerical simulations (DNS) that require discretization in both directions (see, e.g., Malamataris *et al.* 2002; Gao *et al.* 2003; Denner *et al.* 2018; Zhou & Prosperetti 2020b).

A distinct subset of liquid film flow occurs over conical geometries, as when rainwater runs down a cone-shaped roof. Research on this configuration is much less extensive than the well-studied flat-plate case. In this paper, we consider a standard situation in which the cone axis is aligned with gravity, so that the flow along the surface is axisymmetric under a properly imposed upstream condition (figure 1). Industrial examples of this type

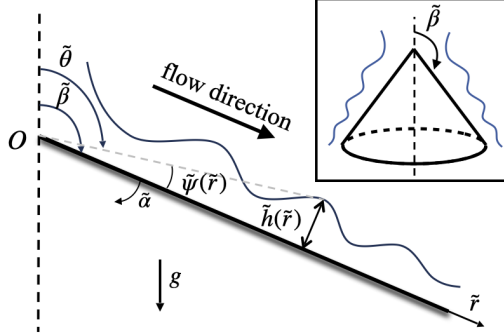


Figure 1: Geometry and coordinate system.

of flow include the Centritherm evaporator and spinning-cone distillation columns (Tanguy *et al.* 2015; Puglisi *et al.* 2022), where the cones may be either rotating or stationary. These systems place high requirements for heat and mass transfer efficiency. As mentioned earlier, the transport processes are significantly influenced by surface wave dynamics. Therefore, investigating the behavior of the liquid film flow on conical surfaces and the accompanying surface waves holds considerable importance.

The dynamics of liquid film flow on a cone differ fundamentally from those on a flat plate. The key feature is the increase in circumference with the radial distance \tilde{r} from the cone apex, which results in an \tilde{r} -dependent local volumetric flow rate per unit width

$$\tilde{Q}_{2D}(\tilde{r}) = \frac{\tilde{Q}}{2\pi\tilde{r} \sin \tilde{\beta}}, \quad (1.4)$$

where \tilde{Q} is the total volumetric flow rate, $90^\circ < \tilde{\beta} < 180^\circ$ is the supplementary of the half-apex angle of the cone (figure 1). A leading-order estimate of the local thickness $\tilde{h}_{N\ell}$ for a steady, gravity-driven liquid film flow can be obtained by substituting Eq. (1.4) into Eq. (1.1) (with $\tilde{\varphi}$ replaced by $\tilde{\beta} - \pi/2$), giving (Zollars & Krantz 1980; Zhou & Prosperetti 2022)

$$\tilde{h}_{N\ell}(\tilde{r}) = - \left(\frac{3\nu\tilde{Q}}{2\pi g\tilde{r} \sin \tilde{\beta} \cos \tilde{\beta}} \right)^{1/3}, \quad (1.5)$$

i.e., in contrast to the Nusselt thickness that is independent of the streamwise coordinate, the undisturbed film thickness on a cone is a function of the radial distance following approximately $\tilde{h}_{N\ell} \propto \tilde{r}^{-1/3}$.

With Eqs. (1.2) and (1.4), the local Reynolds number for the conical liquid film flow is expressed as

$$Re_\ell(\tilde{r}) = \frac{\tilde{Q}}{2\pi\nu\tilde{r} \sin \tilde{\beta}}, \quad (1.6)$$

which is proportional to \tilde{r}^{-1} . Since both the linear and nonlinear behaviors of liquid film flow have a strong dependence on the Reynolds number in the flat-plate situation (see, e.g., Liu *et al.* 1993; Denner *et al.* 2016; Rohlfs *et al.* 2017), these characteristics are expected to vary significantly along a conical surface. Indeed, by doing linear stability analysis, Zollars & Krantz (1980) noted that the phase speed and wavelength of surface waves on a cone decrease with \tilde{r} . They also concluded that unstable disturbances eventually stabilize far from the apex.

This work centers on the dynamics of gravity-driven, axisymmetric liquid film flow on a stationary cone, and develops a model for its numerical simulation. The paper is organized as follows. Section 2 gives the mathematical formulation, where the Navier-Stokes equations and boundary conditions are normalized and truncated. Section 3 derives a Benney-type equation and revisits the linear stability problem, improving the results of Zollars & Krantz (1980) to a second-order accuracy in the small parameter ε (to be introduced in section 2). Section 4 presents a second-order low-dimensional model for efficient simulation of the flow dynamics, which is shown to yield more accurate results compared with the “first-order model” developed earlier by Zhou & Prosperetti (2022). Using this model, for the first time to our knowledge, the spatio-temporal evolution of surface waves on the conical liquid film, including their transition into linear waves, is examined in section 5. Section 6 briefly discusses flow on the upper surface of an inverted cone. Further considerations on the long-wave expansion are provided in section 7. Finally, conclusions are given in section 8.

2. Mathematical formulation

As noted in section 1, thin liquid film flows exhibit a clear scale separation between the streamwise and cross-stream directions. Referred to as the long-wave approximation (Kalliadasis *et al.* 2012), this property has been used to simplify the full Navier-Stokes equations for flow over a flat plate (Benney 1966; Ruyer-Quil & Manneville 2000; Ruyer-Quil *et al.* 2008; Mudunuri & Balakotaiah 2006; Kim & Kim 2024). In this section, we adopt the same strategy to establish the basic framework for subsequent model development. The procedure closely follows Zhou & Prosperetti (2022), but the resultant equations are carried to a higher order with respect to the small parameter to be introduced below.

A spherical coordinate system is employed with the polar axis aligned with the cone axis and the origin O at the apex, see figure 1. This coordinate system is different from that used in Zollars & Krantz (1980), who actually employ a cylindrical coordinate system with its radial axis rotated to align with the cone surface. In the present coordinate system, the polar angle $\tilde{\theta}$ is measured from the upward direction. The cone surface is expressed as $\tilde{\theta} = \tilde{\beta}$; and the radial coordinate \tilde{r} represents the distance from the apex along the wall. For convenience, we introduce the local coordinate $\tilde{\alpha} = \tilde{\theta} - \tilde{\beta}$. The free surface is denoted by $\tilde{\alpha} = \tilde{\psi}$, where $\tilde{\psi}$ is a function of the radial distance \tilde{r} and time \tilde{t} . For the configuration shown in figure 1, $\tilde{\psi}$ is negative. The liquid occupies the region $\tilde{\psi}(\tilde{r}, \tilde{t}) \leq \tilde{\alpha} \leq 0$. The local film thickness $\tilde{h}(\tilde{r}, \tilde{t})$ can be approximated by $-\tilde{r}\tilde{\psi}(\tilde{r}, \tilde{t})$.

Because the flow is axisymmetric, the Navier-Stokes equations in spherical coordinates can be readily simplified. The continuity equation reads

$$\frac{1}{\tilde{r}^2} \frac{\partial}{\partial \tilde{r}} \left(\tilde{r}^2 \tilde{u} \right) + \frac{1}{\tilde{r} \sin \tilde{\theta}} \frac{\partial}{\partial \tilde{\theta}} (\tilde{v} \sin \tilde{\theta}) = 0. \quad (2.1)$$

The momentum equation in the radial direction is

$$\begin{aligned} \frac{\partial \tilde{u}}{\partial \tilde{t}} + \tilde{u} \frac{\partial \tilde{u}}{\partial \tilde{r}} + \frac{\tilde{v}}{\tilde{r}} \frac{\partial \tilde{u}}{\partial \tilde{\theta}} - \frac{\tilde{v}^2}{\tilde{r}} &= -\frac{1}{\rho} \frac{\partial \tilde{p}}{\partial \tilde{r}} - g \cos \tilde{\theta} \\ &+ \nu \left[\frac{1}{\tilde{r}} \frac{\partial^2}{\partial \tilde{r}^2} (\tilde{r} \tilde{u}) + \frac{1}{\tilde{r}^2} \frac{\partial^2 \tilde{u}}{\partial \tilde{\theta}^2} + \frac{\cot \tilde{\theta}}{\tilde{r}^2} \frac{\partial \tilde{u}}{\partial \tilde{\theta}} - \frac{2}{\tilde{r}^2} \frac{\partial \tilde{v}}{\partial \tilde{\theta}} - \frac{2 \tilde{u}}{\tilde{r}^2} - \frac{2 \cot \tilde{\theta}}{\tilde{r}^2} \tilde{v} \right]; \end{aligned} \quad (2.2)$$

and that in the cross-stream direction is

$$\begin{aligned} \frac{\partial \tilde{v}}{\partial \tilde{t}} + \tilde{u} \frac{\partial \tilde{v}}{\partial \tilde{r}} + \frac{\tilde{v}}{\tilde{r}} \frac{\partial \tilde{v}}{\partial \tilde{\theta}} + \frac{\tilde{u} \tilde{v}}{\tilde{r}} &= -\frac{1}{\rho \tilde{r}} \frac{\partial \tilde{p}}{\partial \tilde{\theta}} + g \sin \tilde{\theta} \\ &+ \nu \left[\frac{1}{\tilde{r}} \frac{\partial^2}{\partial \tilde{r}^2} (\tilde{r} \tilde{v}) + \frac{1}{\tilde{r}^2} \frac{\partial^2 \tilde{v}}{\partial \tilde{\theta}^2} + \frac{\cot \tilde{\theta}}{\tilde{r}^2} \frac{\partial \tilde{v}}{\partial \tilde{\theta}} + \frac{2}{\tilde{r}^2} \frac{\partial \tilde{u}}{\partial \tilde{\theta}} - \frac{\tilde{v}}{\tilde{r}^2 \sin^2 \tilde{\theta}} \right], \end{aligned} \quad (2.3)$$

where \tilde{u} and \tilde{v} are the velocity components in the above two directions, respectively. \tilde{p} is pressure; g is gravitational acceleration; ρ and ν represent liquid density and kinematic viscosity, respectively.

On the wall of the cone where $\tilde{\alpha} = 0$, the no-slip condition requires

$$\tilde{u} = \tilde{v} = 0. \quad (2.4)$$

At the free surface of the liquid film, $\tilde{\alpha} = \tilde{\psi}$, the kinematic boundary condition is

$$\frac{\partial \tilde{\psi}}{\partial \tilde{t}} + \tilde{u} \frac{\partial \tilde{\psi}}{\partial \tilde{r}} - \frac{\tilde{v}}{\tilde{r}} = 0; \quad (2.5)$$

the tangential- and normal-stress balances read

$$\tilde{\mathbf{n}} \cdot \tilde{\mathbf{T}} \cdot \tilde{\tau} = 0, \quad (2.6)$$

and

$$\tilde{\mathbf{n}} \cdot \tilde{\mathbf{T}} \cdot \tilde{\mathbf{n}} + \sigma \tilde{C} = 0, \quad (2.7)$$

where $\tilde{\mathbf{T}}$ is the stress tensor, $\tilde{\mathbf{n}}$ and $\tilde{\tau}$ are the unit vectors normal and tangential to the free surface, respectively. σ is the surface tension coefficient; \tilde{C} is the free-surface curvature. In writing Eqs. (2.6) and (2.7), the dynamic effect of the gas phase has been neglected.

Multiplying Eq. (2.1) by $\tilde{r}^2 \sin \tilde{\theta}$ and integrating from $\tilde{\alpha} = 0$ to $\tilde{\alpha} = \tilde{\psi}$ gives

$$\frac{\partial}{\partial \tilde{r}} \left(\int_0^{\tilde{\psi}} \tilde{r}^2 \tilde{u} \sin \tilde{\theta} d\tilde{\alpha} \right) - \tilde{r}^2 \sin \tilde{\theta} \left[\tilde{u} \Big|_{\tilde{\alpha}=\tilde{\psi}} \frac{\partial \tilde{\psi}}{\partial \tilde{r}} - \frac{1}{\tilde{r}} \tilde{v} \Big|_{\tilde{\alpha}=\tilde{\psi}} \right] = 0, \quad (2.8)$$

where the boundary condition Eq. (2.4) has been used. The first term in Eq. (2.8) can be expressed with the volumetric flow rate \tilde{Q} or $\tilde{q} \equiv \tilde{Q}/(2\pi)$, which, by definition, is

$$\tilde{q} = \frac{\tilde{Q}}{2\pi} = \int_{\tilde{\psi}}^0 \tilde{r}^2 \tilde{u} \sin \tilde{\theta} d\tilde{\alpha}. \quad (2.9)$$

Invoking Eq. (2.5), Eq. (2.8) can be rewritten as

$$\frac{\partial \tilde{\psi}}{\partial \tilde{t}} - \frac{1}{\tilde{r}^2 \sin(\tilde{\beta} + \tilde{\psi})} \frac{\partial \tilde{q}}{\partial \tilde{r}} = 0. \quad (2.10)$$

Following Zhou & Prosperetti (2022), we introduce two length scales, H and L , to normalize the film thickness \tilde{h} and radial coordinate \tilde{r} , respectively. The ratio between these two scales is denoted by ε , which is expected to be small:

$$\varepsilon \equiv \frac{H}{L} \ll 1. \quad (2.11)$$

It is noteworthy that $|\tilde{\psi}| \approx \tilde{h}/\tilde{r} \sim H/L = \varepsilon$.

Similarly, we denote the streamwise and cross-stream velocity scales by U and V , respectively. Inserting them into Eq. (2.1) and noting $\partial/\partial \tilde{\theta} = \partial/\partial \tilde{\alpha} \sim \varepsilon^{-1}$ gives $V/U \sim \varepsilon$. The time scale is expressed as the combination L/U , indicating that the temporal variation

occurs together with the liquid transportation in the streamwise direction. For the gravity-driven flow considered currently, the gravitational acceleration is responsible for both the pressure distribution inside the liquid film and the streamwise flow velocity. Therefore, the pressure is normalized by the hydrostatic value ρgH . The velocity scale is expressed as $U = gH^2/\nu$, the form of which corresponds to the Nusselt velocity profile (Pereira & Kalliadasis 2008) for a flat-plate film and, as will be seen, also well represents the order of magnitude of the radial velocity for an undisturbed liquid film flow on a cone.

With the above preparations, we normalize the governing equations (2.1)-(2.3) by writing

$$\tilde{r} = Lr, \quad \tilde{\alpha} = \varepsilon\alpha, \quad \tilde{u} = Uu, \quad \tilde{v} = \varepsilon Uv, \quad \tilde{t} = \frac{Lt}{U}, \quad \tilde{p} = \rho gH p. \quad (2.12)$$

The constant angle $\tilde{\beta} = \beta$ requires no re-scaling.

The results are

$$\frac{\partial}{\partial r} \left(r^2 u \right) + \frac{\partial}{\partial \alpha} (rv) + \varepsilon rv \left(\cot \beta - \varepsilon \alpha \csc^2 \beta \right) = 0, \quad (2.13)$$

$$\begin{aligned} \varepsilon Re \left(\frac{\partial u}{\partial t} + u \frac{\partial u}{\partial r} + \frac{v}{r} \frac{\partial u}{\partial \alpha} \right) &= -\varepsilon \frac{\partial p}{\partial r} - \cos \beta + \varepsilon \alpha \sin \beta + \frac{1}{2} \varepsilon^2 \alpha^2 \cos \beta \\ &+ \varepsilon^2 \frac{1}{r^2} \frac{\partial}{\partial r} \left(r^2 \frac{\partial u}{\partial r} \right) + \frac{1}{r^2} \frac{\partial^2 u}{\partial \alpha^2} + \varepsilon \frac{\cot \beta}{r^2} \frac{\partial u}{\partial \alpha} - \varepsilon^2 \frac{\alpha}{r^2 \sin^2 \beta} \frac{\partial u}{\partial \alpha} - 2 \frac{\varepsilon^2}{r^2} \left(\frac{\partial v}{\partial \alpha} + u \right), \end{aligned} \quad (2.14)$$

and

$$\frac{1}{r} \frac{\partial p}{\partial \alpha} = \alpha \varepsilon \cos \beta + \sin \beta + \varepsilon \left(\frac{1}{r^2} \frac{\partial^2 v}{\partial \alpha^2} + \frac{2}{r^2} \frac{\partial u}{\partial \alpha} \right), \quad (2.15)$$

respectively. In order to achieve a second-order accuracy, Eqs. (2.13) and (2.14) are truncated at $O(\varepsilon^2)$. Whereas it is sufficient to retain terms up to $O(\varepsilon)$ in Eq. (2.15) in all subsequent derivations. We have implicitly assumed $\sin \beta \sim O(1)$, which holds unless β is very close to 0 or π . This restriction renders the equations inapplicable to limiting cases where the liquid films are on the inner or outer surface of a vertical round tube, which demands special treatments (see, e.g., Ruyer-Quil *et al.* 2008; Dietze *et al.* 2020; Dietze 2024).

The Reynolds number appearing in Eq. (2.14) is defined as $Re = UH/\nu = gH^3/\nu^2$, whose order of magnitude is assigned to be $O(1)$. As discussed in Kalliadasis *et al.* (2012), this constraint can be relaxed. The present derivations are expected to be valid for moderate Reynolds numbers with $Re \gtrsim O(1)$.

The boundary conditions (2.4)-(2.7) are normalized in the same manner. Eqs. (2.4) and (2.5) become

$$u = v = 0, \quad (2.16)$$

and

$$\frac{\partial \psi}{\partial t} + u \frac{\partial \psi}{\partial r} - \frac{v}{r} = 0. \quad (2.17)$$

The balance of tangential stress at the free surface $\alpha = \psi$, truncated at $O(\varepsilon^2)$, reads

$$\frac{\partial u}{\partial \alpha} = 2\varepsilon^2 r^2 \frac{\partial \psi}{\partial r} \frac{\partial u}{\partial r} - \varepsilon^2 r \frac{\partial v}{\partial r} + \varepsilon^2 v - 2\varepsilon^2 r \frac{\partial \psi}{\partial r} \frac{\partial v}{\partial \alpha} - 2\varepsilon^2 r \frac{\partial \psi}{\partial r} u. \quad (2.18)$$

The stress balance in the normal direction, accurate to $O(\varepsilon)$, which is sufficient for later use, is

$$p = 2\varepsilon \left(\frac{1}{r} \frac{\partial v}{\partial \alpha} + \frac{u}{r} \right) - \left(\frac{\varepsilon}{Bo} \right) C, \quad (2.19)$$

where $Bo = \rho g H^2 / \sigma$ is the Bond number.

The normalized curvature of the free surface, given by

$$C = \frac{\cot \beta}{r} + \varepsilon \frac{h \cot^2 \beta}{r^2} + \varepsilon \frac{1}{r} \frac{\partial h}{\partial r} + \varepsilon \frac{\partial^2 h}{\partial r^2}, \quad (2.20)$$

is retained to $O(\varepsilon)$ (A detailed derivation of C is provided in Appendix A). The first term in Eq. (2.20) accounts for the lateral curvature induced by the conical geometry. While the last three terms arise from streamwise fluctuations of the free surface.

According to Eq. (2.15) in which the highest order is $O(1)$, the order of Bo in Eq. (2.19) cannot be higher than $O(\varepsilon)$. Considering the surface tension forces are typically large for common liquids (Kalliadasis *et al.* 2012), we assign $Bo \sim O(\varepsilon)$. Keeping this in mind, in the following text wherever Bo appears, we enclose the combination ε/Bo in parentheses and treat it as a single entity of order 1.

Finally, it is noteworthy that the difference between $\tilde{\psi}$ and $-\tilde{h}/\tilde{r}$ is $\tilde{\psi} + \tilde{h}/\tilde{r} = \tilde{\psi} - \tan \tilde{\psi} = O(\tilde{\psi}^3) \sim O(\varepsilon^3)$, which is negligibly small. Replacing $\tilde{\psi}$ with $-\tilde{h}/\tilde{r}$ in Eq. (2.10) yields, in dimensionless form,

$$\frac{\partial h}{\partial t} = -\frac{1}{r \sin(\beta - \varepsilon h/r)} \frac{\partial q}{\partial r}, \quad (2.21)$$

where $q = \tilde{q}/(UHL)$.

3. Spatial linear stability analysis

3.1. Stability threshold

Unlike the flat-plate scenario, the liquid film flow on a conical surface is non-parallel even when the disturbances are absent. This dependence of the base flow on the streamwise coordinate usually demands special consideration in linear stability analysis (Herbert 1997; Govindarajan & Narasimha 1995, 1997; Bertolotti 1997). For the presently studied conical liquid film flow, Zollars & Krantz (1980) derived an asymptotic base-flow solution from the Navier-Stokes equations, and performed a spatial linear stability analysis with respect to axisymmetric disturbances. However, their results only contained the effect of lateral curvature of the gas-liquid interface. The streamwise curvature was not included due to its smaller order of magnitude (see Eq. (2.20)) in their first-order model.

In this section, we revisit the spatial linear stability problem with a similar approach to that of Zollars & Krantz (1980), extending it to second order and paying special attention to the influence of the streamwise curvature. Instead of employing the stream function as is done in Zollars & Krantz (1980), however, the present analysis is based on a Benney-type equation derived below. For liquid film flow on a flat plate, the cut-off wavenumber obtained from the Benney equation (Benney 1966) coincides with that from the long-wave expansion of the Orr-Sommerfeld equation (Kalliadasis *et al.* 2012, section 5.1.5).

We expand the variables $u(r, \alpha, t)$, $v(r, \alpha, t)$, and $p(r, \alpha, t)$ in powers of ε :

$$u = u^{(0)} + \varepsilon u^{(1)} + \varepsilon^2 u^{(2)} + O(\varepsilon^3), \quad (3.1a)$$

$$v = v^{(0)} + \varepsilon v^{(1)} + \varepsilon^2 v^{(2)} + O(\varepsilon^3), \quad (3.1b)$$

$$p = p^{(0)} + \varepsilon p^{(1)} + \varepsilon^2 p^{(2)} + O(\varepsilon^3). \quad (3.1c)$$

Eqs. (3.1) are substituted into Eqs. (2.13)-(2.15). The terms with superscripts (0), (1), and (2) can be solved sequentially. Expressions of these terms are given in Eqs. (B 1)-(B 6) in

Appendix B for reference. Specifically,

$$u^{(0)} = -r^2 \psi^2 \left(\frac{\alpha}{\psi} - \frac{1}{2} \frac{\alpha^2}{\psi^2} \right) \cos \beta. \quad (3.2)$$

In dimensional form, $\tilde{u}^{(0)} = -g \tilde{h}^2 \cos \tilde{\beta} / (2\nu)$ at the free surface $\tilde{\alpha} = \tilde{\psi}$. This justifies the choice of the velocity scale $U = gH^2/\nu$ in section 2.

The solution (3.1a) is substituted into Eq. (2.21) through the definition of \tilde{q} in Eq. (2.9), i.e.,

$$\frac{\partial h}{\partial t} = \frac{1}{r \sin(\beta - \varepsilon h/r)} \frac{\partial}{\partial r} \int_0^{\psi} r^2 \left(u^{(0)} + \varepsilon u^{(1)} + \varepsilon^2 u^{(2)} \right) \sin(\beta + \varepsilon \alpha) d\alpha. \quad (3.3)$$

The integral and derivative operations in the right-hand side (RHS) are straightforward after performing Taylor expansion for the sinusoidal function. The final result, being a little lengthy, is given by Eqs. (B 7)-(B 10) in Appendix B (some of the symbolic manipulations in this paper were carried out using the Python library SymPy 1.13 (Meurer *et al.* 2017)). Eq. (3.3) is the second-order Benney-type equation for liquid film flow along a conical surface.

Next, we seek the steady-state film thickness \bar{h} at fixed flow rate $q = q_s$ by writing

$$\bar{h} = \bar{h}^{(0)} + \varepsilon \bar{h}^{(1)} + \varepsilon^2 \bar{h}^{(2)} + O(\varepsilon^3). \quad (3.4)$$

After replacing h with \bar{h} and setting $\partial \bar{h} / \partial t = 0$ in Eq. (3.3), $\bar{h}^{(0)}$, $\bar{h}^{(1)}$, and $\bar{h}^{(2)}$ are solved successively as

$$\bar{h}^{(0)} = K(q_s/r)^{1/3}, \quad (3.5)$$

$$\bar{h}^{(1)} = -\frac{4K^2 Re q_s^{5/3}}{35r^{8/3} \sin \beta} + \frac{K^2 q_s^{2/3} \sin \beta}{9r^{5/3} \cos \beta} + \frac{K^2 q_s^{2/3} \cos \beta}{3r^{5/3} \sin \beta} - \left(\frac{\varepsilon}{Bo} \right) \frac{K q_s^{1/3}}{3r^{7/3} \sin \beta}, \quad (3.6)$$

and

$$\begin{aligned} \bar{h}^{(2)} = & \frac{19648 Re^2 q_s^3}{121275r^5 \sin^3 \beta \cos \beta} + \frac{32 Re q_s^2}{105r^4 \sin \beta \cos^2 \beta} + \frac{83 Re q_s^2}{140r^4 \sin^3 \beta} - \frac{7q_s \sin \beta}{27r^3 \cos^3 \beta} \\ & - \frac{67q_s}{24r^3 \sin \beta \cos \beta} - \frac{27q_s \cos \beta}{40r^3 \sin^3 \beta} - \frac{7q_s}{40r^3 \sin^3 \beta \cos \beta} \\ & + \left(\frac{\varepsilon}{Bo} \right) \left[-\frac{4K^2 Re q_s^{5/3}}{105r^{14/3} \sin^2 \beta} - \frac{40K^2 q_s^{2/3}}{81r^{11/3} \cos \beta} - \frac{K^2 q_s^{2/3} \cos \beta}{r^{11/3} \sin^2 \beta} + \left(\frac{\varepsilon}{Bo} \right) \frac{2K q_s^{1/3}}{9r^{13/3} \sin^2 \beta} \right], \end{aligned} \quad (3.7)$$

where the constant $K = -\sqrt[3]{3}/(\sin \beta \cos \beta)$ is positive if $\beta > \pi/2$. This base-flow solution is used in the subsequent linear stability analysis. Zollars & Krantz (1976) also derived a first-order asymptotic expression for the steady-state film thickness by applying a perturbation expansion to the stream function. Truncating our result at the same order, i.e., $\bar{h}^{(0)} + \varepsilon \bar{h}^{(1)}$, reproduces their formula once their scaling is adopted. These expressions for \bar{h} are expected to be valid except in the vicinity of the cone axis (see section 7.1 for more discussions).

Before proceeding, it might be interesting to examine the shapes of the undisturbed film flow predicted by Eq. (3.4). However, the dependence of the dimensionless quantities on the unspecified length scales H and L causes inconvenience in displaying results and describing liquid properties/working conditions. It is noteworthy that, H and L (thus ε) are introduced to simplify the governing equations by distinguishing the orders of different terms explicitly. Once the final results, e.g. Eq. (3.4), are obtained, it would be useful to re-nondimensionalize the variables with a more specific length scale such as the film thickness at the inlet, \tilde{h}_{in} , or

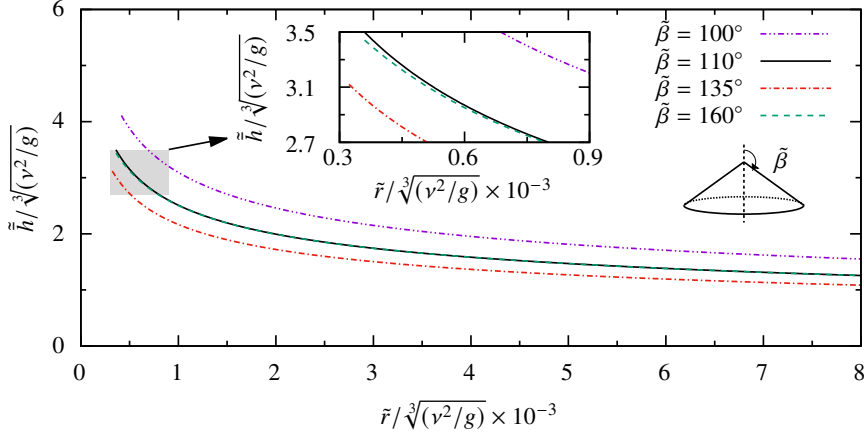


Figure 2: Steady-state film thickness (Eq. (3.4)) versus radial distance at different $\tilde{\beta}$.
 $Ka_{\perp} = 242$, $N_{q\perp} = 1703$.

the combination $(\nu^2/g)^{1/3}$. Actually, on substitution of $L = H = (\nu^2/g)^{1/3}$, one finds

$$Re = \frac{gH^3}{\nu^2} = 1, \quad Bo = \frac{\rho g H^2}{\sigma} = \frac{\rho g^{1/3} \nu^{4/3}}{\sigma} \equiv \frac{1}{Ka_{\perp}}, \quad q = \frac{\tilde{q}}{UHL} = \frac{\tilde{q} g^{1/3}}{\nu^{5/3}} \equiv N_{q\perp}, \quad (3.8)$$

i.e., Re is always 1; the original Bond number converts to a form whose inverse is usually designated to the Kapitza number, Ka_{\perp} ; and the nondimensionalized flow rate q becomes $N_{q\perp}$. The subscript \perp indicates the dimensionless groups are “vertical” versions that are irrelevant to the angle $\tilde{\beta}$.

Figure 2 shows \tilde{h} as a function of \tilde{r} predicted by Eq. (3.4) at four different $\tilde{\beta}$. The other parameters are fixed as $Ka_{\perp} = 242$, and $N_{q\perp} = 1703$. For an aqueous glycerol solution with $\nu = 5.77 \times 10^{-6} \text{ m}^2/\text{s}$ (case C in Denner *et al.* (2018)), this $N_{q\perp}$ corresponds to a dimensional volumetric flow rate of $\tilde{Q} = 2\pi\tilde{q} = 9.28 \times 10^{-6} \text{ m}^3/\text{s}$. Interestingly, all four curves in figure 2 are nearly parallel to each other. With the same volumetric flow rate, the film thickness at the same radial position decreases as $\tilde{\beta}$ increases from 100° to 135° . However, further increasing $\tilde{\beta}$ leads to a higher elevation of the film surface. Moreover, except for the very small region close to the apex, the result with $\tilde{\beta} = 160^\circ$ is almost indistinguishable from that with $\tilde{\beta} = 110^\circ$.

The above observation results from the fact that the corrections $\tilde{h}^{(1)}$ and $\tilde{h}^{(2)}$ to $\tilde{h}^{(0)}$ are negligible unless in regions where r is small (the powers of r in the denominators successively increase from $\tilde{h}^{(0)}$ to $\tilde{h}^{(2)}$, indicating faster decay with r for high-order corrections). As a consequence, the film shape is dominated by $\tilde{h}^{(0)}$ (Eq. (3.5)), which, on substitution of K , yields

$$\tilde{h}^{(0)} = - \left(\frac{3q_s}{r \sin \beta \cos \beta} \right)^{1/3} = - \left[\frac{6q_s}{r \sin(2\beta)} \right]^{1/3}. \quad (3.9)$$

Noting that the dimensional form of Eq. (3.9) is exactly the same as Eq. (1.5). Obviously, Eq. (3.9) indicates that $\tilde{h}^{(0)}(\beta)$ is symmetric about $\beta = 3\pi/4$ or $\tilde{\beta} = 135^\circ$. This explains the overlap of the film surface for $\tilde{\beta} = 110^\circ$ and 160° in figure 2.

This non-monotonic behavior can be interpreted as below: as $\tilde{\beta}$ increases from 90° to 180° , i.e., when the cone becomes progressively sharper, there are two competing mechanisms that can affect the film thickness at a fixed position \tilde{r} . On the one hand, the local volumetric flow rate per unit width is calculated as $\tilde{Q}_{2D} = \tilde{Q}/(2\pi\tilde{r} \sin \tilde{\beta})$, which increases with $\tilde{\beta}$.

Thus, the film thickness also has a tendency to increase. On the other hand, the streamwise component of the gravitational acceleration $-g \cos \tilde{\beta}$ increases. The liquid in the film is therefore accelerated to gain a higher mean velocity, resulting in a thinner film at a fixed flow rate. Consequently, the actual film thickness is determined jointly by the geometric and dynamic factors, which are associated with $\sin \beta$ and $-\cos \beta$ in Eq. (3.9), respectively.

Notably, the existence of a minimal film thickness at a given flow rate might be helpful in designing heat and mass transfer equipment, as a thinner film has a smaller resistance for the transport process between the wall and the gas side.

In order to perform the stability analysis, we express the film thickness as the sum of the base flow and a small disturbance $\hat{h} \ll 1$:

$$h = \bar{h}(r) + \hat{h}(r, t). \quad (3.10)$$

After substitution of Eq. (3.10), Eq. (3.3) can be linearized by dropping all terms containing second- and higher-order powers of \hat{h} . The result is

$$\frac{\partial \hat{h}}{\partial t} + S_0 \hat{h} + S_1 \frac{\partial \hat{h}}{\partial r} + S_2 \frac{\partial^2 \hat{h}}{\partial r^2} + S_3 \frac{\partial^3 \hat{h}}{\partial r^3} + S_4 \frac{\partial^4 \hat{h}}{\partial r^4} = 0. \quad (3.11)$$

The coefficients S_0 - S_4 are given by Eqs. (B 11)-(B 15) in Appendix B.

On the basis of Eq. (3.11), we conduct a spatial linear stability analysis. Assuming the disturbance is periodic in time and grows/decays in space, we set

$$\hat{h}(r, t) = R(r) e^{j\omega t}, \quad (3.12)$$

where j is the imaginary unit, and ω , denoting the dimensionless angular frequency of the disturbance, is a real number. Substitution of Eq. (3.12) into (3.11) leads to an equation for $R(r)$. Following Zollars & Krantz (1980), we assume $R(r)$ is expressed as

$$R(r) = e^{f_0(r) + \varepsilon f_1(r) + \varepsilon^2 f_2(r) + O(\varepsilon^3)}, \quad (3.13)$$

where the functions $f_i(r)$ ($i = 0, 1, 2$) are complex in general and solved sequentially. Their expressions are listed in Eqs. (B 16)-(B 21) of Appendix B. By taking the real part in the final result, \hat{h} reads

$$\hat{h}(r, t) = C \frac{e^{Br}}{r^{1/3}} \cos(\omega t - Ar), \quad (3.14)$$

where

$$A = -[\text{Im}(f_0) + \varepsilon \text{Im}(f_1) + \varepsilon^2 \text{Im}(f_2)]/r, \quad (3.15)$$

$$B = [\varepsilon \text{Re}(f_1) + \varepsilon^2 \text{Re}(f_2)]/r, \quad (3.16)$$

and C is an integral constant. $\text{Re}(\cdot)$ and $\text{Im}(\cdot)$ denote the real and imaginary parts of a complex number, respectively.

It is noteworthy that, at large radial distance r , B is dominated by

$$-\varepsilon^2 \left(\frac{\varepsilon}{Bo} \right) \frac{K^2 \omega^4 r^{7/3} \sin \beta}{270 q_s^{7/3} \cot^2 \beta}, \quad (3.17)$$

which is always negative. Noting Eq. (3.14), this fact indicates that for any given ω , the amplitude of the disturbance \hat{h} decays to zero at large r , i.e., the flow ultimately stabilizes.

Within a certain range of moderate r , however, the disturbances can be amplified locally. Zollars & Krantz (1980) classified the instability of this non-parallel flow into two types: the absolute growth refers to the scenario in which the raw disturbance amplitude increases with r , i.e., $d[\exp(Bo)/r^{1/3}]/dr > 0$; whereas the relative growth means an increase of the

amplitude scaled by the local mean film thickness \bar{h} whose value is given in Eq. (3.4), i.e., $d[\exp(Br)/(\bar{h}r^{1/3})]/dr > 0$. Correspondingly, two modified spatial amplification factors can be defined as

$$G_a \equiv \frac{1}{\exp(Br)/r^{1/3}} \frac{d[\exp(Br)/r^{1/3}]}{dr} = r \frac{dB}{dr} + B - \frac{1}{3r} \quad (3.18)$$

for absolute growth and

$$G_r \equiv \frac{1}{\exp(Br)/(\bar{h}r^{1/3})} \frac{d[\exp(Br)/(\bar{h}r^{1/3})]}{dr} = r \frac{dB}{dr} + B - \frac{1}{\bar{h}} \frac{\partial \bar{h}}{\partial r} - \frac{1}{3r} \quad (3.19)$$

for relative growth (the definition of G_r differs from that in Zollars & Krantz (1980)). The difference between the two expressions is the term $-(\partial \bar{h}/\partial r)/\bar{h}$, which is positive since \bar{h} is negatively correlated with r , see Eq. (3.5). Therefore, this term has a destabilizing effect, and it is possible that at the same r , a flow is stable in the sense of absolute growth ($G_a < 0$), yet unstable in the sense of relative growth ($G_r > 0$).

Figure 3 shows the neutral stability curves in the parameter space spanned by the disturbance angular frequency $\tilde{\omega}$ and radial coordinate \tilde{r} . The stability thresholds for absolute ($G_a = 0$) and relative ($G_r = 0$) growth are represented by solid and dashed lines, respectively. The thick gray curves show second-order results. The blue curves are obtained by inserting the first-order ($O(\varepsilon)$) expressions of B and \bar{h} into Eqs. (3.18) and (3.19), i.e., with the order of accuracy achieved in Zollars & Krantz (1980). For both absolute and relative growth, a dependence of the stability thresholds on the radial distance is observed. Any disturbance will be stabilized at sufficiently large \tilde{r} , as expected. Compared with the first-order result, the second-order neutral curves for both instabilities shift toward the small \tilde{r} region, especially at high disturbance frequencies.

In fact, the difference between the first- and second-order results primarily originates from the term $\varepsilon \partial^2 h / \partial r^2$ in Eq. (2.20), which essentially represents the contribution of streamwise curvature of the free surface. The expressions of G_a and G_r with only this additional second-order correction read

$$G_a = -\varepsilon \frac{2Re\omega^2}{15 \cos \beta} - \varepsilon \frac{4\sqrt[3]{3}Req_s^{4/3}}{3r^{10/3} \sin^{4/3} \beta \cos^{1/3} \beta} - \varepsilon \frac{\omega^2 r \sin^2 \beta}{9q_s \cos^2 \beta} + \varepsilon \frac{8\sqrt[3]{3}q_s^{1/3} \sin^{2/3} \beta}{27r^{7/3} \cos^{4/3} \beta} + \varepsilon \frac{8\sqrt[3]{3}q_s^{1/3} \cos^{2/3} \beta}{9r^{7/3} \sin^{4/3} \beta} - \frac{1}{3r} + \varepsilon \left(\frac{\varepsilon}{Bo} \right) \frac{2}{3r^3 \sin \beta} - \varepsilon^2 \left(\frac{\varepsilon}{Bo} \right) \frac{3^{2/3} \omega^4 r^{7/3} \sin^{7/3} \beta}{81q_s^{7/3} \cos^{8/3} \beta}, \quad (3.20)$$

and

$$G_r = -\varepsilon \frac{2Re\omega^2}{15 \cos \beta} - \varepsilon \frac{16\sqrt[3]{3}Req_s^{4/3}}{15r^{10/3} \sin^{4/3} \beta \cos^{1/3} \beta} - \varepsilon \frac{\omega^2 r \sin^2 \beta}{9q_s \cos^2 \beta} + \varepsilon \frac{\sqrt[3]{3} \sqrt[3]{q_s} \sin^{2/3} \beta}{9r^{7/3} \cos^{4/3} \beta} + \varepsilon \frac{11\sqrt[3]{3}q_s^{1/3} \cos^{2/3} \beta}{27r^{7/3} \sin^{4/3} \beta} + \varepsilon \frac{\sqrt[3]{3}q_s^{1/3}}{27r^{7/3} \sin^{4/3} \beta \cos^{4/3} \beta} - \varepsilon^2 \left(\frac{\varepsilon}{Bo} \right) \frac{3^{2/3} \omega^4 r^{7/3} \sin^{7/3} \beta}{81q_s^{7/3} \cos^{8/3} \beta}. \quad (3.21)$$

The stability thresholds calculated with these simplified versions of G_a and G_r (red lines in figure 3) are nearly indistinguishable from the full second-order results (gray lines). In conclusion, the streamwise curvature has a significant influence in stabilizing the liquid film flow on a conical surface, confirming the speculation of Zollars & Krantz (1980) who did not, however, provide the corresponding formulae or quantitative results.

Moreover, further comparison (results not shown here) reveals that the effect of the lateral curvature, i.e., the term $\cot \beta / r$ in Eq. (2.20), is negligible. The reason why the seemingly

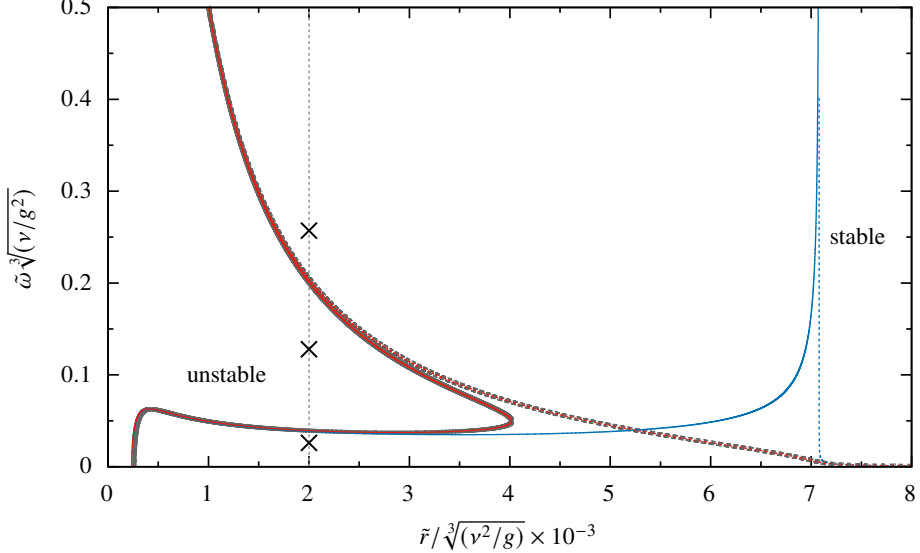


Figure 3: Neutral stability curves for absolute (solid lines) and relative (dashed lines) growth in the parameter space spanned by disturbance angular frequency $\tilde{\omega}$ and radial distance \tilde{r} ; $\tilde{\beta} = 150^\circ$, $Ka_\perp = 242$, and $N_{q\perp} = 1703$. Gray lines: second-order model; blue lines: first-order model; red lines: first-order formulae plus second-order streamwise-curvature correction. The three symbols correspond to the cases shown in figure 6.

smaller streamwise curvature (second-order) has a higher impact than the first-order lateral curvature will be further discussed in section 7.2.

A noteworthy feature of the absolute-growth threshold is its multi-valued dependence on \tilde{r} : over a finite radial interval, the flow is stable at both low and high disturbance frequencies, and unstable only at intermediate values. Another observation from figure 3 is the overlapping of the absolute and relative growth thresholds when $\tilde{\omega}$ is large. At small $\tilde{\omega}$, the flow can be stable for absolute growth but unstable for relative growth, as anticipated earlier. This is understandable as, since the film thickness decreases with \tilde{r} , it is more stringent for a flow to be stable in the sense of relative growth.

3.2. Wavelength and phase speed for linear waves

According to Eq. (3.14), the phase of a linear wave is $\phi = \omega t - Ar$, where A is a function of r . Therefore, following a fixed phase with $d\phi = \omega dt - [d(Ar)/dr]dr = 0$, the phase speed is calculated as

$$c = \left[\frac{dr}{dt} \right]_{d\phi=0} = \frac{\omega}{d(Ar)/dr}. \quad (3.22)$$

The lines in figure 4 show c as functions of \tilde{r} , computed with Eq. (3.22). The polar angle is $\tilde{\beta} = 150^\circ$. The Kapitza number is $Ka_\perp = 242$. From left to right, the dimensionless volumetric flow rates are $N_{q\perp} = 851.5$, 1703 , and 3000 , respectively. The corresponding dimensionless disturbance angular frequencies, defined as $N_{\omega\perp} = \tilde{\omega}(\nu/g^2)^{1/3}$, are 0.108 , 0.128 , and 0.148 . A remarkable characteristic is that the lines are nearly straight with a slope of $-2/3$ in the logarithm coordinates. Indeed, inserting the leading-order part of Eq. (3.15)

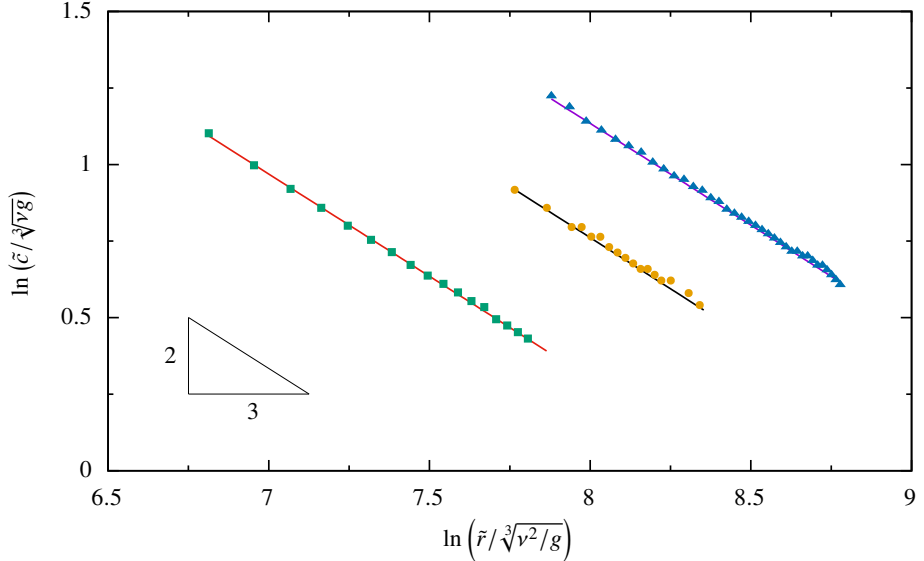


Figure 4: Phase speed of linear waves versus distance from cone apex; $\tilde{\beta} = 150^\circ$, $Ka_\perp = 242$. Lines: Eq. (3.22); symbols: h - q model (section 4). Squares: $N_{q\perp} = 851.5$, $N_{\omega\perp} = 0.108$; circles: $N_{q\perp} = 1703$, $N_{\omega\perp} = 0.128$; triangles: $N_{q\perp} = 3000$, $N_{\omega\perp} = 0.148$.

into Eq. (3.22) yields

$$c^{(0)} = \frac{3q_s^{2/3}}{Kr^{2/3} \sin \beta} \propto r^{-2/3}. \quad (3.23)$$

The leading-order wavelength can be calculated accordingly following $\lambda^{(0)} = 2\pi c^{(0)}/\omega$, which shares the same power law. The value of $c^{(0)}$ is $3/5$ times the phase speed in Zollars (1974) (Eq. (VI-17)), if the same scaling is used. This difference arises because the latter used A instead of $d(Ar)/dr$ as the local wavenumber.

In addition, it would be useful to nondimensionalize the phase speed with the Nusselt scaling (Kalliadasis *et al.* 2012) and compare the results with the flat-plate situation. In that scaling, the characteristic velocity is chosen as $\tilde{h}_{N2D}^2/(l_\nu t_\nu)$, where \tilde{h}_{N2D} is the Nusselt film thickness defined in Eq. (1.1). The viscous-gravity length and time scales are $l_\nu = [\nu^2/(g \sin \tilde{\beta})]^{1/3}$ and $t_\nu = [\nu/(g \sin \tilde{\beta})^2]^{1/3}$, respectively. For the current conical scenario, we apply a modified Nusselt scaling by replacing \tilde{h}_{N2D} with the leading-order approximation to the local base-flow film thickness $\tilde{h}_{N\ell}$, see Eq. (1.5). In this way, the velocity scale is written as $\tilde{h}_{N\ell}^2/(l_\nu t_\nu)$, with the length and time scales

$$l_\nu = \left(\frac{\nu^2}{-g \cos \tilde{\beta}} \right)^{1/3}, \quad \text{and} \quad t_\nu = \left(\frac{\nu}{g^2 \cos^2 \tilde{\beta}} \right)^{1/3}, \quad (3.24)$$

respectively (the relation $\tilde{\beta} = \pi/2 + \tilde{\varphi}$ has been used). With this nondimensionalization, Eq. (3.23) yields a leading-order phase speed of

$$c'^{(0)} = \frac{\tilde{c}^{(0)}(\tilde{r}) l_\nu t_\nu}{\tilde{h}_{N\ell}^2(\tilde{r})} \equiv 1, \quad (3.25)$$

which is irrelevant to \tilde{r} . This value is identical to the leading-order flat-plate result. The same conclusion, however, does not hold for the first- and second-order components, in which the

present conical results contain \tilde{r} -dependent terms. That being said, when taking $\tilde{r} \rightarrow \infty$, the present expressions exactly reduce to the flat-plate ones obtained with spatial-mode stability analysis. In particular, the first-order correction is $\tilde{c}_{2D}^{(1)} = 0$, while the second-order component, in dimensional form, is

$$\tilde{c}_{2D}^{(2)} = -\frac{2\nu\tilde{\omega}^2 \sin^2 \tilde{\beta}}{9g \cos^3 \tilde{\beta}} + \frac{\nu\tilde{\omega}^2}{g \cos \tilde{\beta}} - \frac{2\tilde{\omega}^2 \tilde{Q}_{2D} \sin \tilde{\beta}}{35g \cos^2 \tilde{\beta}} + \frac{44\tilde{\omega}^2 \tilde{Q}_{2D}^2}{175g\nu \cos \tilde{\beta}}. \quad (3.26)$$

4. Second-order $h\text{-}q$ model

Unlike the flat-plate case, the dependence of the flow field on the streamwise coordinate prohibits the use of periodic boundary conditions on a single wave unit. An alternative to efficiently simulate the nonlinear waves is the low-dimensional models. Recently, Zhou & Prosperetti (2022) derived a “first-order” $h\text{-}q$ model via the Galerkin method (see, e.g., Ruyer-Quil & Manneville 2000; Scheid *et al.* 2006) to study hydraulic jumps. Notably, their model is not purely first order, as it includes the second-order contribution of the streamwise curvature, see Eq. (3.21) in Zhou & Prosperetti (2022). The Galerkin method has proven to be the most efficient in obtaining the “optimal” low-dimensional model for liquid film flow on a flat plate (Ruyer-Quil & Manneville 2000). Here we extend the model in Zhou & Prosperetti (2022) to full second order in ε for more accurate surface wave simulations.

Starting from the truncated cross-stream momentum equation (2.15), we integrate from $\alpha = 0$ to ψ , invoke the continuity equation (2.13) and boundary conditions (2.16) and (2.19), obtaining the first-order pressure distribution

$$p = r(\alpha - \psi) \sin \beta + \frac{1}{2}\varepsilon r \left(\alpha^2 - \psi^2 \right) \cos \beta - \varepsilon \left. \left(\frac{\partial u}{\partial r} + 2\frac{u}{r} \right) \right|_{\psi} - \left(\frac{\varepsilon}{Bo} \right) C. \quad (4.1)$$

Inserting Eq. (4.1) into the streamwise momentum equation (2.14) yields the second-order boundary-layer equation

$$\begin{aligned} \varepsilon Re \left(\frac{\partial u}{\partial t} + u \frac{\partial u}{\partial r} + \frac{v}{r} \frac{\partial u}{\partial \alpha} \right) &= \frac{1}{r^2} \frac{\partial^2 u}{\partial \alpha^2} + \varepsilon \frac{\cot \beta}{r^2} \frac{\partial u}{\partial \alpha} + \varepsilon^2 \left(2 \frac{\partial^2 u}{\partial r^2} + \frac{4}{r} \frac{\partial u}{\partial r} + \frac{2}{r^2} u \right) \\ &- \varepsilon^2 \frac{\alpha}{r^2 \sin^2 \beta} \frac{\partial u}{\partial \alpha} - \cos \beta + \varepsilon \sin \beta \left(\psi + r \frac{\partial \psi}{\partial r} \right) + \varepsilon \left(\frac{\varepsilon}{Bo} \right) \frac{\partial C}{\partial r} + \frac{1}{2} \varepsilon^2 \cos \beta \psi^2 \\ &+ \varepsilon^2 r \cos \beta \psi \frac{\partial \psi}{\partial r} + \varepsilon^2 \frac{\partial}{\partial r} \left[\left. \left(\frac{\partial u}{\partial r} + 2\frac{u}{r} \right) \right|_{\psi} \right]. \end{aligned} \quad (4.2)$$

Next, we apply the Galerkin method to Eq. (4.2). Guided by the leading-order profile Eq. (3.2), the trial function for the streamwise velocity is constructed as a semi-parabolic function of the cross-stream coordinate:

$$u^* \equiv mF = m \left[2\frac{\alpha}{\psi} - \left(\frac{\alpha}{\psi} \right)^2 \right]. \quad (4.3)$$

The coefficient m is irrelevant to α , but may depend on the streamwise coordinate r and time t . It is determined by substituting Eq. (4.3) into the dimensionless form of Eq. (2.9). The result, retained up to $O(\varepsilon^2)$, reads

$$m = -\frac{3}{2} \frac{q}{r^2 \psi \sin \beta} \left[1 - \varepsilon \frac{5}{8} \psi \cot \beta + \varepsilon^2 \left(\frac{9}{40} \psi^2 + \frac{25}{64} \psi^2 \cot^2 \beta \right) \right]. \quad (4.4)$$

Eq. (4.2) can be formally written as $\mathcal{L}(u) = 0$. With the trial function u^* , the residual across the film is

$$\mathcal{R} = \int_0^\psi F \mathcal{L}(u^*) d\alpha, \quad (4.5)$$

where F defined in Eq. (4.3) serves as the test function.

It is noteworthy that the boundary condition in Eq. (2.18) is non-homogeneous, whereas $\partial^2 u^* / \partial \alpha^2 \equiv 0$. Therefore, u^* satisfies Eq. (2.18) only to the order of $O(\varepsilon)$. To recover the missing $O(\varepsilon^2)$ constraint, we embed Eq. (2.18) through the second-order α -derivative in Eq. (4.5). In detail, the integral of the term $F \partial^2 u^* / \partial \alpha^2$ is re-expressed via Green's second identity (or, equivalently, by applying the integration by parts twice) as

$$\int_0^\psi F \frac{\partial^2 u^*}{\partial \alpha^2} d\alpha = \left(F \frac{\partial u^*}{\partial \alpha} \right) \Big|_0^\psi - \left(\frac{\partial F}{\partial \alpha} u^* \right) \Big|_0^\psi + \int_0^\psi \frac{\partial^2 F}{\partial \alpha^2} u^* d\alpha. \quad (4.6)$$

The value $[\partial u^* / \partial \alpha]_\psi$ in the first term of the RHS is replaced by Eq. (2.18), thus the latter is involved in the derivation. A similar method is applied to develop the second-order low-dimensional model for the flat-plate case (Ruyer-Quil & Manneville 2000).

Inserting Eq. (4.6), eliminating $\partial h / \partial t$ with Eq. (2.21), and requiring $\mathcal{R} = 0$ yields:

$$\begin{aligned} & \varepsilon Re \left(1 + \varepsilon \frac{5h \cot \beta}{8r} \right) \frac{\partial q}{\partial t} + \frac{\varepsilon Re}{r \sin \beta} \left(\frac{17q}{7h} \frac{\partial q}{\partial r} - \frac{9q^2}{7h^2} \frac{\partial h}{\partial r} - \frac{9q^2}{7rh} \right) \\ & + \frac{\varepsilon^2 Re \cos \beta}{r^2 \sin^2 \beta} \left(\frac{5167q}{1792} \frac{\partial q}{\partial r} - \frac{1557q^2}{1792h} \frac{\partial h}{\partial r} - \frac{4203q^2}{1792r} \right) \\ = & - \frac{5rh \sin \beta \cos \beta}{6} - \frac{5q}{2h^2} - \varepsilon \left(\frac{5rh \sin^2 \beta}{6} \frac{\partial h}{\partial r} + \frac{5q \cot \beta}{2rh} \right) + \varepsilon \left(\frac{\varepsilon}{Bo} \right) \frac{5rh \sin \beta}{6} \frac{\partial C}{\partial r} \quad (4.7) \\ & + \varepsilon^2 \left[\frac{5h^2 \sin \beta \cos \beta}{6} \frac{\partial h}{\partial r} + \frac{9}{2} \frac{\partial^2 q}{\partial r^2} - \frac{6q}{h} \frac{\partial^2 h}{\partial r^2} - \frac{9}{2h} \frac{\partial h}{\partial r} \frac{\partial q}{\partial r} + \frac{4q}{h^2} \left(\frac{\partial h}{\partial r} \right)^2 \right. \\ & \left. - \frac{5h^3 \sin \beta \cos \beta}{12r} - \frac{9}{2r} \frac{\partial q}{\partial r} + \frac{19q}{4rh} \frac{\partial h}{\partial r} - \frac{7q}{4r^2} - \frac{2q}{r^2 \sin^2 \beta} \right]. \end{aligned}$$

Eqs. (2.21) and (4.7) describe the evolution of the film thickness h and volumetric flow rate q , respectively. These two partial differential equations constitute the second-order low-dimensional model (referred to as the h - q model hereafter) for the liquid film flow on a cone. The model recovers to the “first-order” one proposed by Zhou & Prosperetti (2022) by dropping all $O(\varepsilon^2)$ terms except for those representing the streamwise surface tension contribution. On the other hand, by substituting $q_{2D} = q / (r \sin \beta)$, replacing β with $\pi/2 + \varphi$, and taking the limit $r \rightarrow \infty$, Eqs. (2.21) and (4.7) become

$$\frac{\partial h}{\partial t} = - \frac{\partial q_{2D}}{\partial x}, \quad (4.8)$$

and

$$\begin{aligned} Re \frac{\partial q_{2D}}{\partial t} = & - \frac{17Re q_{2D}}{7h} \frac{\partial q_{2D}}{\partial x} + \frac{9Re q_{2D}^2}{7h^2} \frac{\partial h}{\partial x} + \frac{5h \sin \varphi}{6} - \frac{5q_{2D}}{2h^2} - \varepsilon \frac{5h \cos \varphi}{6} \frac{\partial h}{\partial x} \\ & + \varepsilon^2 \left[\frac{9}{2} \frac{\partial^2 q_{2D}}{\partial x^2} - \frac{6q_{2D}}{h} \frac{\partial^2 h}{\partial x^2} - \frac{9}{2h} \frac{\partial h}{\partial x} \frac{\partial q_{2D}}{\partial x} + \frac{4q_{2D}}{h^2} \left(\frac{\partial h}{\partial x} \right)^2 + \left(\frac{\varepsilon}{Bo} \right) \frac{5h}{6} \frac{\partial^3 h}{\partial x^3} \right], \quad (4.9) \end{aligned}$$

respectively, where the coordinate r is replaced by x for consistency. Eqs. (4.8) and (4.9) are

identical to the simplified second-order model for the thin liquid film flow over an inclined plate (Ruyer-Quil & Manneville 2000).

The coupled equations (2.21) and (4.7) can be readily advanced in time on a uniform one-dimensional mesh in the radial direction. For time stepping, we use the Bogacki–Shampine method (Bogacki & Shampine 1989), a second/third-order adaptive Runge–Kutta method. The timestep is automatically adjusted to control the estimated local error below the specified tolerance. With the (normalized) values of h and q being of order $\gtrsim O(1)$ in our simulations, we set an absolute tolerance of 10^{-6} . The spatial derivatives are discretized with central finite difference schemes accurate at least to second order. The film thickness h_{in} and volumetric flow rate q_{in} are specified at the inlet r_{in} of the computational domain. In order to facilitate the transition of the flow towards a fully developed state, for a given q_{in} and r_{in} , h_{in} is estimated from Eq. (3.5). Zero-gradient conditions for h and q are imposed at the outlet, which is sufficiently far from the region of interest.

As a validation of both the model and code, we compare the numerical results with those obtained from the linear theory of section 3. A periodic disturbance is imposed at the inlet on q_{in} :

$$q = q_{\text{in}} [1 + \zeta \cos(2\pi f t)], \quad (4.10)$$

where f and ζ are the frequency and relative amplitude of the disturbance, respectively. We set $\zeta = 10^{-7}$ to create small-amplitude surface waves within the linear regime. The phase speed c at different r is extracted from the wave profiles. In detail, the oscillatory component \hat{h} is determined by subtracting \bar{h} from the computed film thickness, see Eq. (3.10). Then, the local phase speed is calculated as the speed of the wave peaks in $\hat{h}(r, t)$. The result (solid symbols in figure 4) agree closely with the theoretical prediction (solid lines) from Eq. (3.22).

The ability of the h - q model in predicting neutral stability curves is examined in figure 5(a), where it can be seen that, for both absolute and relative growth, the numerical results of the h - q model (symbols) have a good consistency with the linear-theory prediction (lines).

For reference, the shape of the film surface for a typical case is illustrated in figure 5(b), where the small-amplitude linear waves can be barely observed at this scale. The inset shows the isolated \hat{h} following Eq. (3.10). The position where the flow is neutrally stable is determined by seeking the local maximum (marked by the vertical dashed line) or minimum of the oscillations' envelope.

Moreover, we display the linear wave profiles near a fixed radial distance with different frequencies in figure 6. From panels (a) to (c), the normalized disturbance angular frequencies are $N_{\omega \perp} = 0.026, 0.128$, and 0.257 , respectively. With the same radial distance $\tilde{r}/\sqrt[3]{(v^2/g)} \times 10^{-3} = 2$, the locations of the three selected situations in the $\tilde{\omega}$ - \tilde{r} space are marked by the three symbols in figure 3. According to figure 3, at this radius, the flow is stable at $N_{\omega \perp} \equiv \tilde{\omega} \sqrt[3]{v/g^2} = 0.026$, unstable at $N_{\omega \perp} = 0.128$, and is stable again at $N_{\omega \perp} = 0.257$. This is indeed true as can be observed from the growth/decay tendency of the wave envelops depicted in figure 6.

The h - q model is further validated in terms of its performance in simulating large-amplitude nonlinear waves. The results of the model are compared against those of DNS, which is conducted using the interFoam solver embedded in the OpenFOAM-v2412 software. By employing a volume-of-fluid method, the liquid film is fully resolved in both the streamwise and cross-stream directions. For the present axisymmetric simulation, the computational domain is a wedge with an angle of 3° and one grid layer in the circumferential direction. The number of cells in the cross-stream direction is typically 48. The cell aspect ratio is set to less than three. Therefore, depending on the length of the computational domain, the cell number in the streamwise direction ranges from 5000 to 16000. The Crank–Nicolson method is used for time marching. The linear-upwind and van Leer schemes are used for

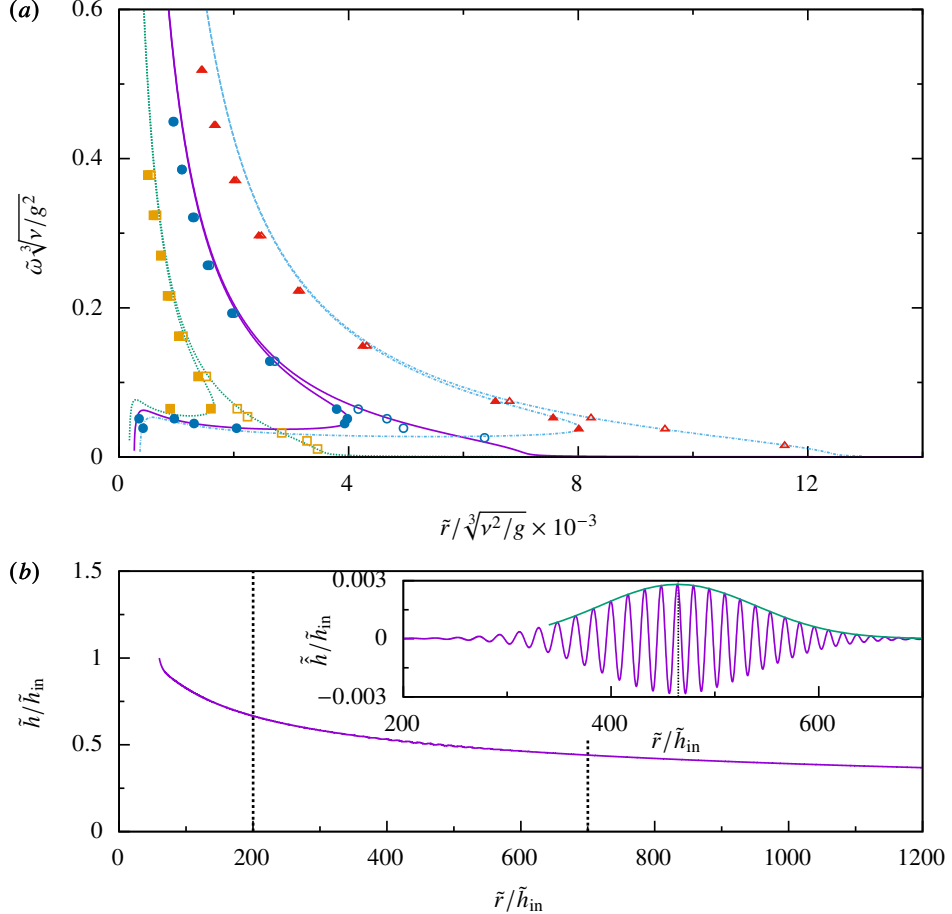


Figure 5: (a) Neutral stability curves; $\tilde{\beta} = 150^\circ$ and $Ka_\perp = 242$. The volumetric flow rates for dashed, solid, and dash-dotted lines are $N_{q\perp} = 851.5, 1703$, and 3000 , respectively. For each case, the curves on the left and right correspond to absolute and relative growth, respectively. Symbols (solid: absolute growth; open: relative growth) mark transition positions extracted from h - q model results. (b) Instantaneous film thickness of a case in panel (a). Inset illustrates how the neutral stability position is determined.

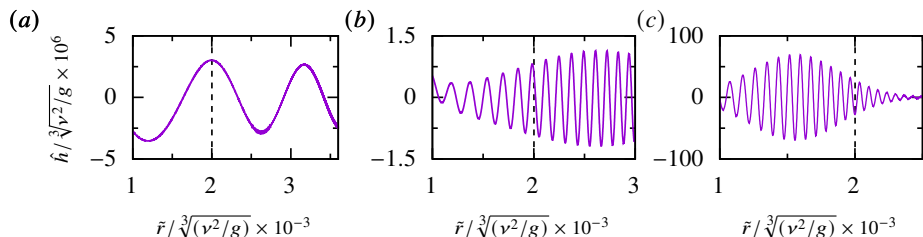


Figure 6: Oscillatory part of the film thickness simulated using the h - q model. $\tilde{\beta} = 150^\circ$, $Ka_\perp = 242$, and $N_{q\perp} = 1703$. From (a) to (c), $N_{\omega\perp} = 0.026, 0.128$, and 0.257 , respectively.

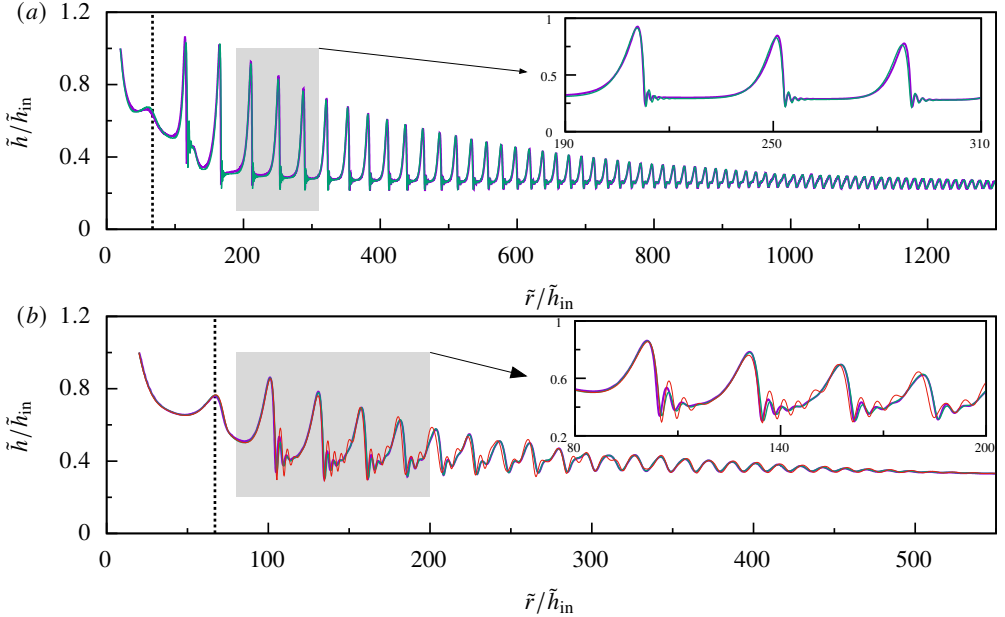


Figure 7: Film thickness versus distance from cone apex at $Ka_{\perp} = 242$. (a) $\tilde{\beta} = 135^\circ$, $N_{q\perp} = 17490$, $N_{\omega\perp} = 0.197$; (b) $\tilde{\beta} = 110^\circ$, $N_{q\perp} = 11242$, $N_{\omega\perp} = 0.172$. Purple lines: DNS; green lines: second-order h - q model. The red line in panel (b) is obtained with the “first-order” model of Zhou & Prosperetti (2022). The vertical dashed lines mark the positions where $\tilde{h}_{N\ell}/\tilde{r} = 0.01$.

spatial discretization of the convective terms in the momentum equations and the equation for phase fraction evolution, respectively. The computation is second-order accurate in both time and space.

Figure 7 shows the instantaneous shape of the free surface for two cases with large-amplitude waves. The horizontal coordinate has been highly compressed to more clearly display the surface deformation. The results of DNS and the h - q model are denoted by purple and green lines, respectively. The waves are generated by setting ζ in Eq. (4.10) to a relatively large value, typically 0.05. For the case shown in panel (a), $\tilde{\beta} = 135^\circ$, $N_{q\perp} = 17490$, and $N_{\omega\perp} = 0.197$. For panel (b), $\tilde{\beta} = 110^\circ$, $N_{q\perp} = 11242$, and $N_{\omega\perp} = 0.172$. In both cases, $Ka_{\perp} = 242$.

Figure 7(a) illustrates a representative case in which solitary waves occur near the inlet. These waves are characterized by a large main hump and several preceding small capillary ripples within a wave unit. The steeper slopes render these solitary waves more challenging in numerical simulations than small-amplitude smooth waves. For this case, a mesh-converged solution requires the number of cells being around 10000 for the h - q model. With this mesh resolution, there are about 350 mesh cells within a single wavelength near the inlet. In particular, the capillary ripples ahead of the big hump are resolved with 10-15 cells. As \tilde{r} increases, the waves convert into sinusoidal-shaped waves whose amplitudes are much smaller. Throughout the entire computational domain, the result of the h - q model is in good agreement with the DNS data. Notably, for this case, the computational time of the model on a single CPU core is less than 10% of the DNS simulation, which was conducted in parallel using 64 CPU cores, showing a speedup of two to three orders of magnitude with comparable computational resources.

Figure 7(b) presents a different case in which the main humps of the solitary waves are

milder in amplitude. The result of the “first-order” model developed in Zhou & Prosperetti (2022) is also shown (red line). Both models perform well in the sinusoidal-wave region. However, in the solitary-wave region, the first-order model incorrectly predicts more capillary waves with larger amplitudes. Kalliadasis *et al.* (2012, p. 72) reported a similar improvement of the second-order model over the first-order one in predicting capillary ripples within the flat-plate scenario. They attributed this difference to the inclusion of second-order viscous terms in the second-order model. As a matter of fact, the first-order model developed in Zhou & Prosperetti (2022) is numerically unstable for the case shown in figure 7(a), unless sufficient numerical viscosity is artificially added (Zhou & Prosperetti 2022). However, for all cases shown in this paper, no special treatment is needed for the second-order model developed in section 4.

The dimensionless parameters for the case in figure 7(a) can describe a film flow of a 45% (w/w) aqueous glycerol solution with $\rho = 1113 \text{ kg/m}^3$, $\nu = 5.77 \times 10^{-6} \text{ m}^2/\text{s}$, and $\sigma = 59.7 \times 10^{-3} \text{ N/m}$. These liquid properties are identical to those in Case C of Denner *et al.* (2018). The volumetric flow rate is $\tilde{Q} = 9.53 \times 10^{-5} \text{ m}^3/\text{s}$. The disturbance frequency is $\tilde{f} = 8 \text{ Hz}$. The positions of the inlet and outlet of the computational domain, when converted into dimensional values, are $\tilde{r}_{\text{in}} \approx 0.026 \text{ m}$ and $\tilde{r}_{\text{out}} \approx 1.66 \text{ m}$. The steady-state film thicknesses, based on Eq. (1.5), are $\tilde{h}_{N\ell}(\tilde{r}_{\text{in}}) = 1.28 \text{ mm}$ and $\tilde{h}_{N\ell}(\tilde{r}_{\text{out}}) = 0.32 \text{ mm}$, respectively. Correspondingly, the local Reynolds number Re_ℓ , according to Eq. (1.6), decreases from 145 at $\tilde{r} = \tilde{r}_{\text{in}}$ to 2.2 at $\tilde{r} = \tilde{r}_{\text{out}}$. Figure 7 demonstrates that, although the h - q model is formulated under the assumption that $Re \sim O(1)$, its accuracy remains acceptable at significantly higher local Reynolds numbers up to the order of $O(10)$ - $O(100)$.

It would be beneficial to compare the h - q model results with experimental data. As the literature on wavy liquid film flow along conical surfaces are quite limited. We evaluate the conical model’s performance at the flat-plate limit, which requires $r \rightarrow \infty$. In practice, this is achieved by placing the computational domain in a region where r is extremely large (taken as $\tilde{r}/\tilde{h}_{\text{in}} > 10^9$ in our simulations). The wave shapes obtained in this way are compared with experimental results in figure 8, where the parameters of the six flat-plate cases are the same as those shown in figure 9 of Denner *et al.* (2018). The DNS results reported in the same paper are also extracted and plotted for reference. As can be seen, within the range of $Re_{2D} \sim O(10)$ (panels (a), (b), and (d)), the model results are consistent with the experimental data as well as the DNS results. For higher Reynolds numbers (Re_{2D} approaching $O(100)$), the h - q model can still reasonably predict the shape of the main humps, although it fails to accurately capture the capillary ripples.

5. Spatio-temporal evolution of surface waves

In this section, the spatio-temporal evolution of surface waves is further investigated by using the h - q model developed in section 4 (Eqs. (2.21) and (4.7)), which has been shown to be much more efficient than DNS while retaining comparable accuracy.

5.1. Morphology of surface waves

The instantaneous profiles in figure 7 reveal some important characteristics of the waves. Similar to the linear-theory prediction in section 3.2, the wavelength decreases with the distance from the cone apex. This is accompanied with the damping of the wave amplitude. The waves become shorter and weaker, eventually diminishing at large \tilde{r} . This phenomenon is also consistent with the linear result in section 3, where it is shown that the film flow is stable at large radial distances, see figure 3. For small \tilde{r} , the waves are solitary; as \tilde{r} increases, a transition to sinusoidal-shaped waves is observed.

The contour map in figure 9 shows the spatio-temporal evolution of the waves for a

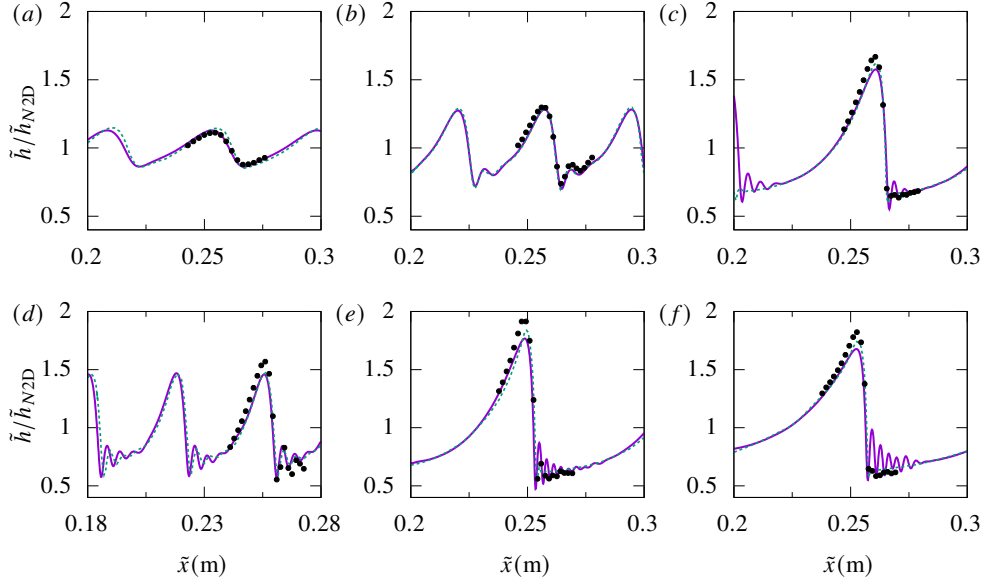


Figure 8: Film thickness versus streamwise coordinate. The experimental data (symbols) and DNS results (green dashed lines) are extracted from the corresponding panels of figure 9 in Denner *et al.* (2018); the purple solid lines show the results obtained with the present conical h - q model in the large- r limit. For each panel, horizontal translation is applied for the best match between the present results and those from the original figure.

From (a) to (f), $Re_{2D} = 5.2, 7.5, 20.6, 12.4, 45.1$, and 77.0 , respectively.

representative case we have simulated. The film thickness is indicated by brightness, so that the wave peaks can be traced following the bright lines in the figure. The instantaneous shape of the free surface corresponding to $\tilde{t} = 0$ is presented on the bottom.

The phase speed of the waves, as can be deduced from the slopes of the bright lines in figure 9, is also a decreasing function of \tilde{r} . This trend is also the same as that of linear waves, see figure 4. The more curved bright lines at smaller \tilde{r} indicate larger decreasing rates of the phase speed. This is because the liquid film spreads out and thins more significantly due to the conical geometry in small- \tilde{r} regions. At sufficiently large radial distance, the variation of flow characteristics with \tilde{r} becomes mild; the film flow approaches the flat-plate limit described by Eqs. (4.8) and (4.9).

For a more systematic examination, we conducted simulations with $\tilde{\beta}$ ranging from 100° to 150° with an increment of 5° . The other parameters are set to $Ka_\perp = 242$, $N_{q\perp} = 11242$, and $N_{\omega\perp} = 0.221$. These values are selected to be moderate, allowing observation of different types of surface waves as $\tilde{\beta}$ is varied. Three representative cases are selected from the results with successively increasing angles $\tilde{\beta} = 110^\circ$, 130° , and 150° , see figure 10. The green dashed lines represent undisturbed free surfaces. Both the radial and cross-stream coordinates are nondimensionalized by the film thickness \tilde{h}_{in} at the inlet. As can be seen, steeper cones produce larger wave amplitude near the axis, with more solitary waves observed before the waves become sinusoidal. The number of capillary ripples ahead of the main hump also increases (see insets). An interesting observation is that, although the steady-state film thickness decreases with \tilde{r} , the envelop of the wave troughs is nearly parallel to the cone surface.

The phase speeds of the surface waves for the three cases shown in figure 10 are presented in figure 11(a). The symbols are extracted from the results of h - q model at discrete radial

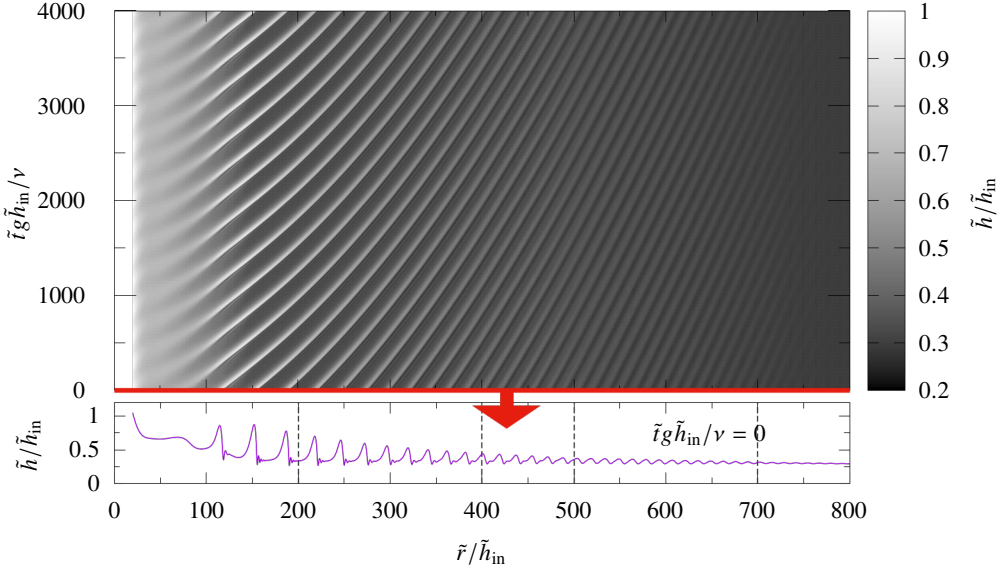


Figure 9: Contour map of the spatio-temporal evolution of surface waves; $\tilde{\beta} = 120^\circ$, $Ka_\perp = 240$, $N_{q\perp} = 12084$, and $N_{\omega\perp} = 0.177$. The inlet is located at $\tilde{r}_{\text{in}}/\tilde{h}_{\text{in}} = 20$. Brightness indicates local film thickness. The instantaneous free surface profile at $\tilde{t}g\tilde{h}_{\text{in}}/\nu = 0$ is presented on the bottom. The vertical dashed lines show the positions where the data in the four panels of figure 12 are extracted.

positions. The straight lines show the leading-order predictions from linear theory, Eq. (3.23), whose dimensional form reads

$$\tilde{c}^{(0)} = \left(\frac{3\tilde{Q}}{2\pi\tilde{r} \sin \tilde{\beta}} \right)^{2/3} \left(-\frac{g \cos \tilde{\beta}}{\nu} \right)^{1/3}. \quad (5.1)$$

For all three cases, the phase speed agrees with the linear theory at sufficiently large \tilde{r} , coinciding with the observation in figure 10 that the waves convert to small-amplitude linear waves eventually. In the region where \tilde{r} is small, however, different behaviors are observed: the waves in figure 10(a) have more pronounced depression, with phase speeds smaller than the leading-order solution of linear waves. These are the characteristics of the γ_1 -type waves, or slow waves, defined by Chang *et al.* (1993a,b). On the contrary, the waves close to the inlet in figure 10(c) are elevation dominant, with phase speeds larger than those of linear waves. These are γ_2 -type waves, or fast waves, according to Chang *et al.* (1993a,b).

The occurrence of γ_1 and γ_2 waves in different cases can be interpreted with the neutral curves in figure 11(b), where the disturbance frequency for the cases in figure 10 is shown by the horizontal dash-dotted line. Liu *et al.* (1993) found that on a flat plate, γ_1 waves appear when the forcing frequency is just below the cut-off frequency; whereas γ_2 waves emerge at still lower frequencies. As illustrated in figure 11(b), at a given \tilde{r} , the cut-off angular frequency $\tilde{\omega}$ increases with $\tilde{\beta}$. Therefore, γ_2 waves are more likely to be observed when $\tilde{\beta}$ is large.

In the flat-plate situation, γ_1 waves are unstable (Kalliadasis *et al.* 2012, p. 271) and easily switch to γ_2 waves with presence of forced inlet disturbances (Liu & Golub 1994). However, this secondary instability can be suppressed on a conical surface: figure 11(b) shows that as \tilde{r} increases, the range of unstable $\tilde{\omega}$ narrows. Therefore, disturbances capable of triggering

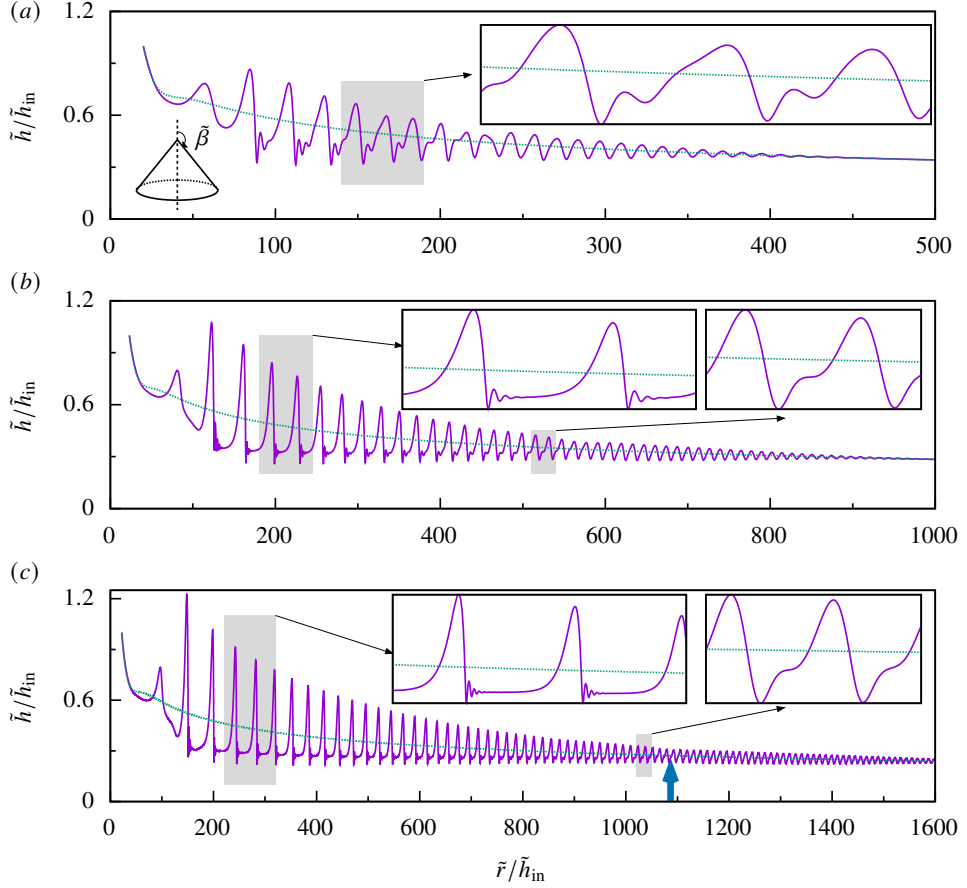


Figure 10: Instantaneous wave profiles for $\tilde{\beta} = 110^\circ$ (a), 130° (b), and 150° (c). $Ka_\perp = 242$, $N_{q\perp} = 11242$, and $N_{\omega\perp} = 0.221$. Dashed lines show undisturbed free surfaces obtained with the h - q model. The blue arrow in panel (c) marks the position of the turning point in figure 14. A depiction of $\tilde{\beta}$ is displayed in panel (a).

the secondary instabilities may not have sufficient time to amplify before they are damped. Consequently, for small $\tilde{\beta}$, the entire free surface can be dominated by γ_1 waves (figure 10a), whereas for large $\tilde{\beta}$, a transition from γ_2 to γ_1 waves may occur (figure 10c, also see the purple lines and symbols in figure 11a).

5.2. Transition from solitary to sinusoidal waves

As shown in section 5.1, the surface waves undergo a transition from solitary to sinusoidal-like profiles. Considering the importance of wave shapes in pertinent heat- and mass-transfer processes (see, e.g., Miyara 1999, 2000a; Aktershev *et al.* 2022), we elaborate on this transition in detail.

The top panels of figures 12(a-d) present the instantaneous film thickness versus time at four fixed downstream positions with $\tilde{r}/\tilde{h}_{in} = 200, 400, 500$, and 700 , respectively. The case is identical to that shown in figure 9, in which the four positions are indicated by vertical dashed lines. The bottom panels show the corresponding Fast Fourier Transform (FFT) spectra based on the periodic time series. The amplitudes are normalized by their sum for all non-zero frequency components. The red arrows mark the disturbance frequency imposed

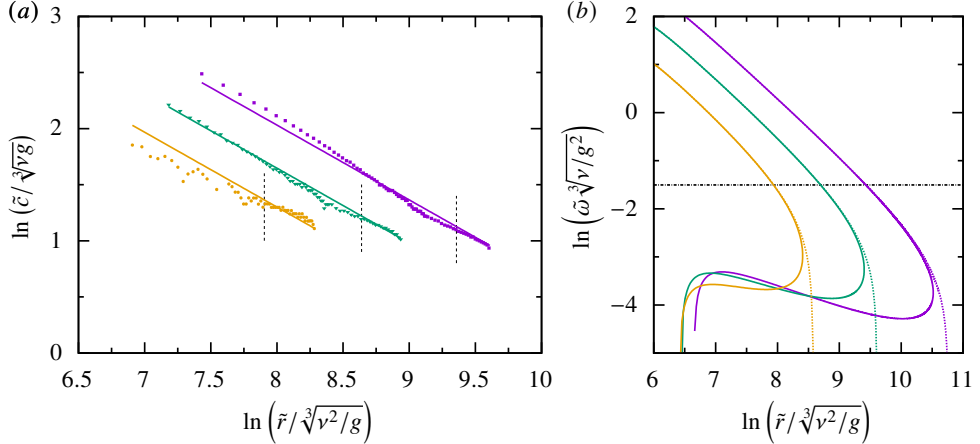


Figure 11: (a) Phase speed versus radial distance. Yellow, green, and purple symbols represent the results of h - q model for cases in figures 10(a), 10(b), and 10(c), respectively. Straight lines of the same color display the leading-order phase speed predicted by linear theory. Vertical dashed lines mark positions where the normalized fundamental-frequency amplitude exceeds 90% (section 5.2). (b) Neutral curves of absolute (solid) and relative (dashed) growth. The color scheme is the same as in panel (a). The horizontal dash-dotted line shows the disturbance angular frequency $N_{\omega\perp} = 0.221$.

at the inlet. At $\tilde{r}/\tilde{h}_{\text{in}} = 200$, the waves are solitary, producing multiple spectral peaks in the FFT results. Further downstream, the wave shape smooths with fewer fluctuations in time. Correspondingly, the number of visible components in the FFT results decreases, with the fundamental frequency becoming more pronounced. At $\tilde{r}/\tilde{h}_{\text{in}} = 700$, the temporary wave evolution is almost sinusoidal. The spectrum is dominated by the fundamental frequency, with most high-order harmonics diminishing.

The transition from solitary to sinusoidal waves is found to exhibit a close correlation with the linear stability threshold. Figure 13 shows the neutral curves of absolute (solid lines) and relative (dashed lines) growth for cases with different apex angles and liquid properties. The symbols of the same colors mark the positions where the normalized fundamental spectral amplitude exceeds 90% at given disturbance frequencies. As can be observed, all symbols roughly align with the neutral curve for relative growth, indicating that the position where sinusoidal waves appear on a conical surface—if a 90%-amplitude criterion is employed—can be estimated by the position from which the flow becomes stable in the relative sense. Consequently, when other parameters are fixed, a higher forcing frequency promotes the transition from solitary to sinusoidal waves.

In figure 11(a), the radial positions of the 90%-amplitude threshold are indicated by short vertical dashed lines. Clearly, the phase speeds coincide with the linear predictions to the right of these dashed lines. Therefore, the solitary-sinusoidal wave transition also signals the transition from nonlinear to linear waves. Indeed, the typical amplitude of the sinusoidal waves observed in our numerical simulations is as small as about 0.2% of the local wavelength.

Figure 14 shows the phase speed (a) and wave peak height (b) versus \tilde{r} for the case in figure 10(c). The peak height is nondimensionalized as $\tilde{h}_p/\tilde{h}_{N\ell} - 1$, where $\tilde{h}_{N\ell}$ is the local Nusselt film thickness given by Eq. (1.5). For this representative case, the entire domain can be divided into three distinct regions that are characterized by presence of γ_2 , γ_1 , and sinusoidal waves, respectively. The typical wave profiles in each region are displayed in the insets of panel (b). Near the inlet, the forcing frequency lies well below the local cut-off value.

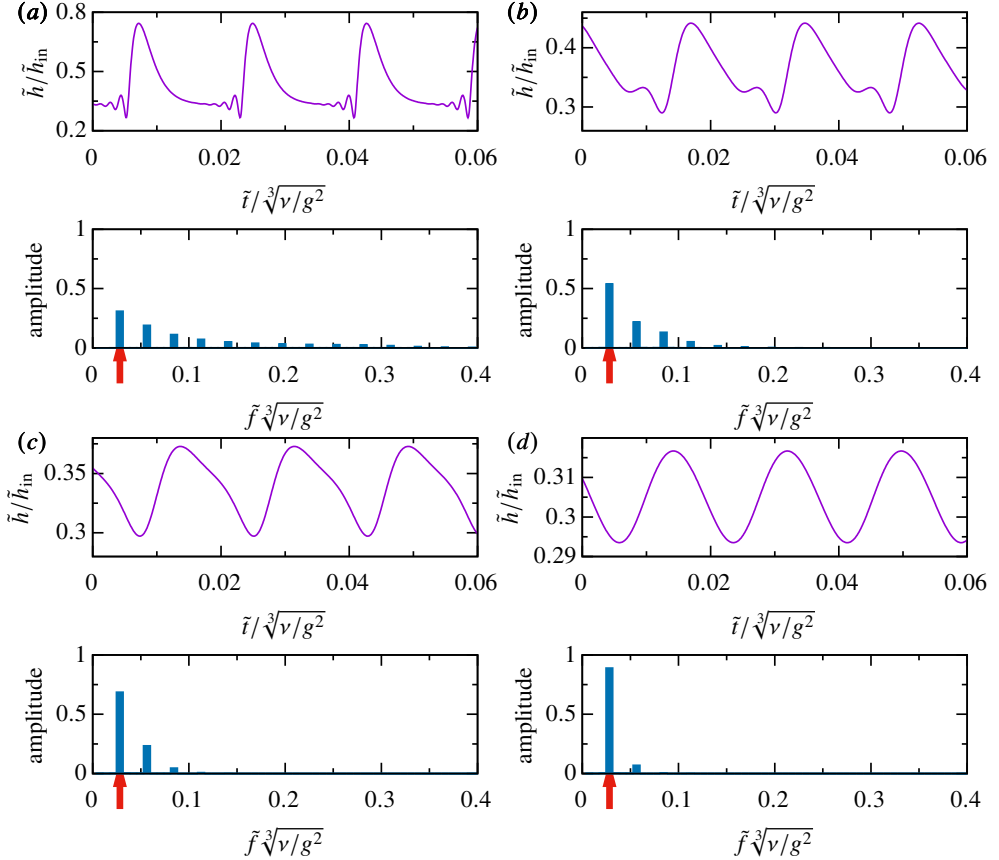


Figure 12: Top panels show temporal evolution of film thickness at four radial positions for the case in figure 9. From (a) to (d), $\tilde{r}/\tilde{h}_{in} = 200, 400, 500$, and 700 , respectively.

Bottom panels: corresponding normalized spectra (DC component removed). Red arrows indicate frequency of imposed disturbance at inlet.

γ_2 waves develop and travel downstream, with their phase speeds larger than the leading-order linear solution (dashed line in panel a). At a larger \tilde{r} , the computed and linear phase speeds cross, signaling the transition from γ_2 to γ_1 waves. Further downstream, the 90%-amplitude criterion divides the solitary and sinusoidal wave regions. The position, based on the FFT result, is $\tilde{r}/\tilde{h}_{in} \approx 1500$. The linear theory predicts a relative growth threshold of $\tilde{r}/\tilde{h}_{in} \approx 1618$. The relative error between the two values is less than 8%.

During the entire evolution process, the capillary ripples preceding the main hump diminish successively. The positions where their number drops are marked by crosses in figure 14(b). Right after the last capillary wave disappears, the trend of the peak height variation experiences a sudden change at about $\tilde{r}/\tilde{h}_{in} = 1086$ (black circle). This turning point is also marked in figure 10(c) (blue arrow). Figure 15 presents the normalized amplitude of the fundamental frequency as a function of \tilde{r} . It experiences a significant shift around the turning point (dashed line), as indicated by the black arrow. Considering the correspondence between the fundamental-frequency amplitude and wave profiles, the turning point can be regarded as the onset of solitary-to-sinusoidal transition. This will be further evidenced in section 5.3.

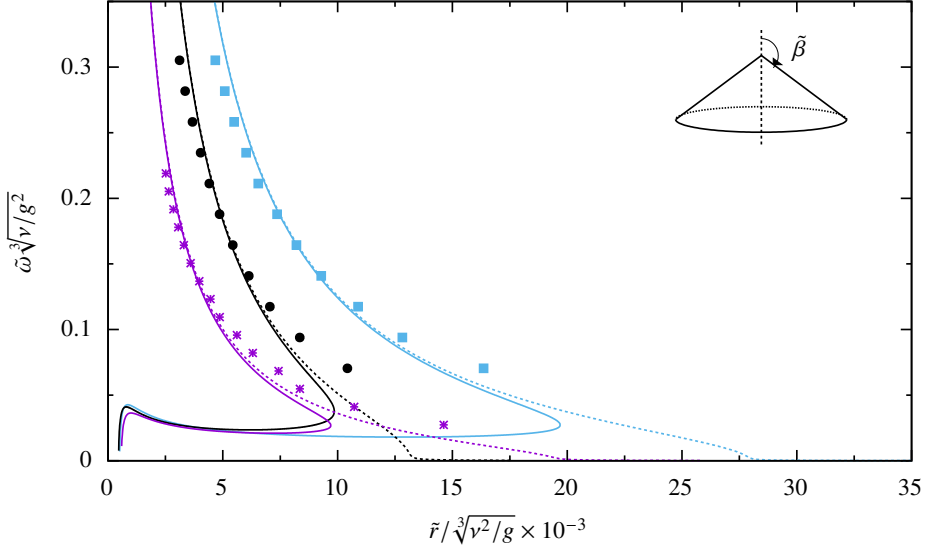


Figure 13: Dimensionless disturbance angular frequency versus radial distance. Lines represent neutral curves for absolute (solid) and relative (dashed) growth from linear theory. Purple: $\tilde{\beta} = 135^\circ$, $Ka_\perp = 3388$, $N_{q\perp} = 11507$; black: $\tilde{\beta} = 135^\circ$, $Ka_\perp = 332$, $N_{q\perp} = 7762$; blue: $\tilde{\beta} = 150^\circ$, $Ka_\perp = 332$, $N_{q\perp} = 6722$. Symbols of the same colors mark the transition positions where the fundamental frequency amplitude exceeds 90%. A depiction of $\tilde{\beta}$ is also displayed.

5.3. Peak height and phase speed of surface waves

For nonlinear two-dimensional solitary waves on a falling liquid film along a vertical plate, Nosoko *et al.* (1996) proposed empirical correlations for the wave peak height \tilde{h}_p and phase speed \tilde{c} , which are

$$N_{hp\perp} = 0.49 Ka_\perp^{-0.132} N_{\lambda\perp}^{0.39} Re_{2D\perp}^{0.46}, \quad (5.2)$$

and

$$N_{c\perp} = 1.13 Ka_\perp^{-0.06} N_{\lambda\perp}^{0.31} Re_{2D\perp}^{0.37}, \quad (5.3)$$

respectively. In Eqs. (5.2) and (5.3), the vertical version of the viscous-gravity length and time scales mentioned earlier, $l_{\nu\perp} = (\nu^2/g)^{1/3}$ and $t_{\nu\perp} = (\nu/g^2)^{1/3}$, are employed for nondimensionalization, i.e.,

$$N_{hp\perp} = \tilde{h}_p / l_{\nu\perp}, \quad N_{\lambda\perp} = \tilde{\lambda} / l_{\nu\perp}, \quad N_{c\perp} = \tilde{c} t_{\nu\perp} / l_{\nu\perp}. \quad (5.4)$$

The Kapitza number $Ka_\perp = \sigma / (\rho \nu^{4/3} g^{1/3})$ has been defined in section 3. The Reynolds number $Re_{2D\perp}$ takes the form of Eq. (1.2) with $\tilde{\varphi} = \pi/2$ in this vertical-plate situation.

Eqs. (5.2) and (5.3) have shown good consistency with DNS results (see, e.g., Miyara 2000b; Zhou & Prosperetti 2020b). To apply these correlations to the conical geometry, we (i) replace g with its streamwise component $-g \cos \tilde{\beta}$, so that l_{ν} and t_{ν} in Eq. (3.24) are used instead of $l_{\nu\perp}$ and $t_{\nu\perp}$ in Eq. (5.4), and Ka_\perp is changed to $Ka = \sigma / [\rho \nu^{4/3} (-g \cos \tilde{\beta})^{1/3}]$; (ii) use the local Reynolds number Re_ℓ (Eq. (1.6)) instead of the constant Re_{2D} . This leads to

$$N_{hp} = 0.49 Ka^{-0.132} N_\lambda^{0.39} Re_\ell^{0.46}, \quad (5.5)$$

and

$$N_c = 1.13 Ka^{-0.06} N_\lambda^{0.31} Re_\ell^{0.37}. \quad (5.6)$$

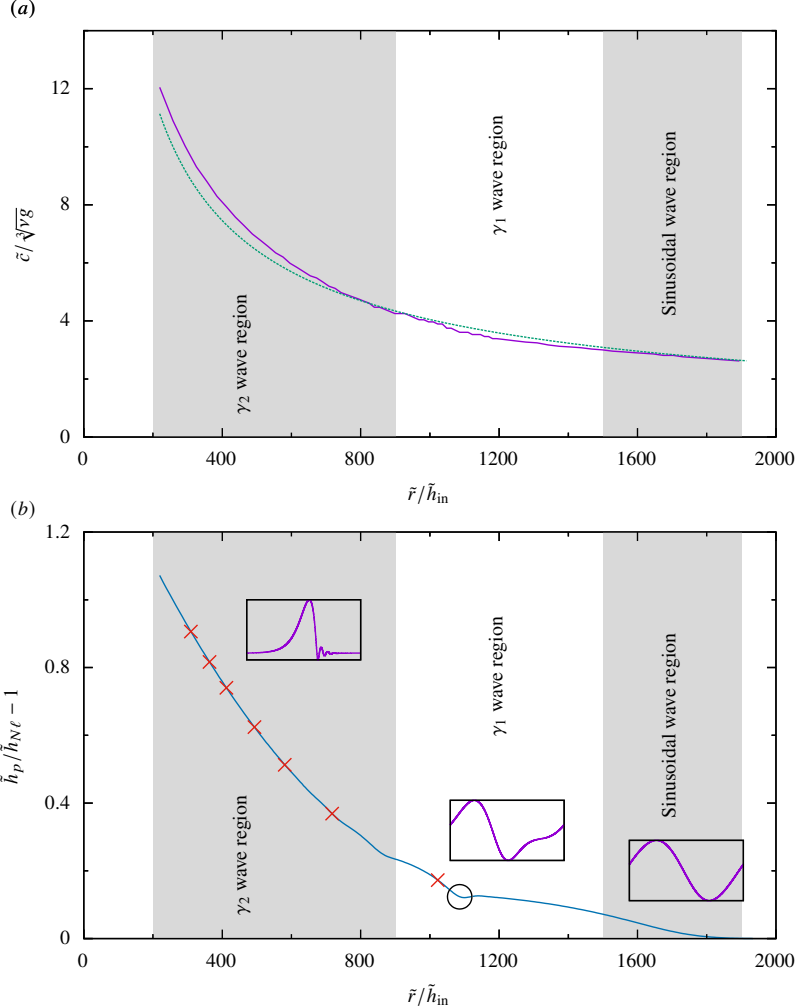


Figure 14: Phase speed (a) and wave peak height (b) versus radial distance for the case in figure 10(c). Dashed line in panel (a): leading-order phase speed from linear theory. Crosses in panel (b): positions where the number of capillary ripples decreases. The black circle highlights the turning point of the curve. The insets show typical wave profiles in different regions.

Figure 16 compares Eqs. (5.5) and (5.6) with the results of h - q model. The data are extracted at different discrete radial coordinates within the fully developed region, covering a relatively wide range of N_{hp} and N_c . In figure 16(a), the wave peak height N_{hp} calculated with Eq. (5.5) agrees well with the numerical result, with the largest relative error less than 6%. The consistency is also acceptable for the phase speed N_c as shown in figure 16(b), especially in the high- N_c region. According to figure 14(a), the waves in this region are solitary waves.

The slight discrepancy at low N_c therefore arises partly because Nosoko *et al.*'s correlation was obtained in the solitary-wave regime; whereas the phase speed in solitary and sinusoidal regions exhibits different behaviors (figure 11a). A similar mismatch was also reported by Miyara (2000a) for high-frequency, non-solitary wave cases. In addition, Nosoko *et al.*'s experiments were conducted for $14 \leq Re_\ell \leq 90$, whereas the data in figure 16 fall in the

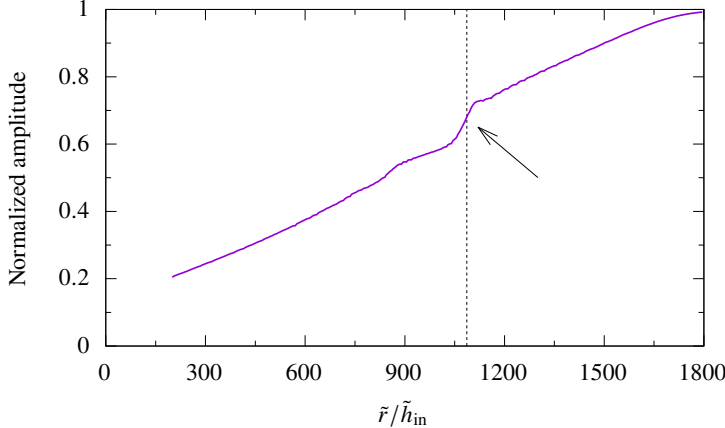


Figure 15: Normalized amplitude of the fundamental frequency versus radial distance for the case in figure 10(c). Vertical dashed line shows the position of turning point identified in figure 14(b).

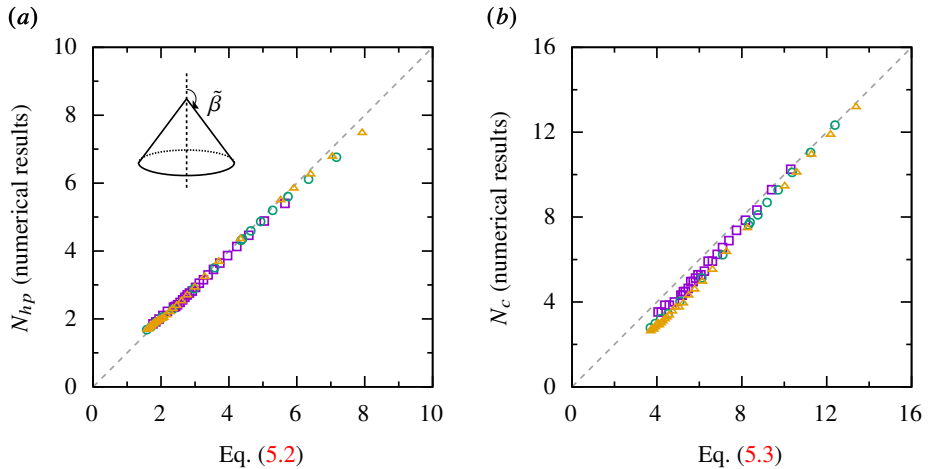


Figure 16: Comparison of peak height (a) and phase speed (b) between the h - q model results and Eqs. (5.5) and (5.6); $Ka_{\perp} = 240$ and $N_{\omega_{\perp}} = 0.177$ for all cases. Purple squares: $N_{q_{\perp}} = 12084$, $\tilde{\beta} = 120^\circ$; green circles: $N_{q_{\perp}} = 13954$, $\tilde{\beta} = 135^\circ$; yellow triangles: $N_{q_{\perp}} = 12084$, $\tilde{\beta} = 150^\circ$. The dashed diagonal lines represent the points where the values on the horizontal and vertical axes are equal. A depiction of $\tilde{\beta}$ is displayed in panel (a).

range $Re_{\ell} \lesssim 15$. In any case, it is convenient to refit Eq. (5.6) with the present numerical data. Since it has been shown in section 5.2 that the wave profiles before and after the turning point have different trends, only the data before the turning point are used for fitting. The resultant correlation is

$$N_c = 0.9Ka_{\perp}^{-0.052}N_{\lambda}^{0.26}Re_{\ell}^{0.58}. \quad (5.7)$$

In the comparison shown in figure 16, the wavelength $\tilde{\lambda} = \tilde{\lambda}(\tilde{r})$ is extracted from the

numerical results by measuring the distance between two neighboring wave peaks. This \tilde{r} -dependent wavelength is unknown a prior in practice, which renders the correlations descriptive rather than predictive. Therefore, it is useful to replace the wavelength with the wave frequency, which is constant and known in the current scenario. We define $N_f = \tilde{f}_t$, as the dimensionless forcing frequency. By using the relation $\tilde{c}(\tilde{r}) = \tilde{f}\tilde{\lambda}(\tilde{r})$, whose dimensionless form is $N_c = N_f N_\lambda$, N_λ in Eq. (5.7) can be eliminated. The result is

$$N_c = 0.87Ka^{-0.07}N_f^{-0.35}Re_\ell^{0.78}. \quad (5.8)$$

Accordingly, with Eq. (5.8), Eq. (5.5) can be rewritten as

$$N_{hp} = 0.46Ka^{-0.16}N_f^{-0.53}Re_\ell^{0.76}. \quad (5.9)$$

Since $Re_\ell \propto 1/\tilde{r}$ (see Eq. (1.6)), N_c and N_{hp} also decay with \tilde{r} following $N_c \propto \tilde{r}^{-0.78}$ and $N_{hp} \propto \tilde{r}^{-0.76}$.

Figure 17 shows the peak height (a) and phase speed (b) versus \tilde{r} for four cases in log-log coordinates. Good agreement between the results of h - q model (symbols) and predictions of Eqs. (5.8) and (5.9) (solid lines) is observed up to the turning points that can be easily located in the figures. The result of Eq. (5.1) is shown with dashed lines in figure 17(b). The 90%-amplitude positions mentioned in section 5.2 are marked with short vertical dashed lines for each case. As in figure 11(a), the linear phase speed coincides well with the numerical results in the sinusoidal-wave region.

In conclusion, the waves ahead of the turning point are solitary and carry preceding capillary ripple(s); their peak height and phase speed can be described by correlations (5.8) and (5.9). Beyond the 90%-amplitude location, the waves are small-amplitude and sinusoidal, and their phase speed can be estimated by linear theory. The waves between these two positions exhibit transient behavior.

6. Liquid film flow on the upper surface of an inverted cone

In some industrial applications, such as spinning cone column distillation (see, e.g., Makarytchev *et al.* 2001; Puglisi *et al.* 2022), the liquid film exists on the upper surface of a downward-pointing inverted cone. The geometric configuration is depicted in figure 18, with the polar angle $\tilde{\beta}$ ranging from 0° to 90° . In this situation, the liquid driven by gravity flows toward the direction in which \tilde{r} decreases, so the volumetric flow rate defined in Eq. (2.9) is negative. Because spatial stability is evaluated in the flow direction, the amplification factors, Eqs. (3.18) and (3.19), are replaced by

$$G'_a = -G_a, \quad G'_r = -G_r, \quad (6.1)$$

respectively. Using the simplified expressions, Eqs. (3.20) and (3.21), one finds

$$G'_r(-q_s, \pi - \beta) \equiv G_r(q_s, \beta). \quad (6.2)$$

Thus, at the same inclination, the relative-growth stability thresholds for divergent ($\beta > \pi/2$) and convergence ($\beta < \pi/2$) configurations are identical. As an intermediate situation, the flat-plate liquid film flow is expected to behave similarly (noting that there is no difference between concepts of absolute and relative growth in that situation). This is confirmed in figure 19, where the relative growth neutral curves for the cone (green dashed line), inverted cone (purple dashed line), and flat plate (red dashed line) are indistinguishable when the inclination angles are the same. Indeed, by substituting $\tilde{q}_s = \tilde{q}_{2D}\tilde{r} \sin \tilde{\beta}$, G_r in Eq. (3.21) reduces to the flat-plate growth rate plus some $O(\tilde{r}^{-2})$ terms that decay rapidly as \tilde{r} increases.

In contrast, the absolute-growth neutral curves differ markedly between the situations of

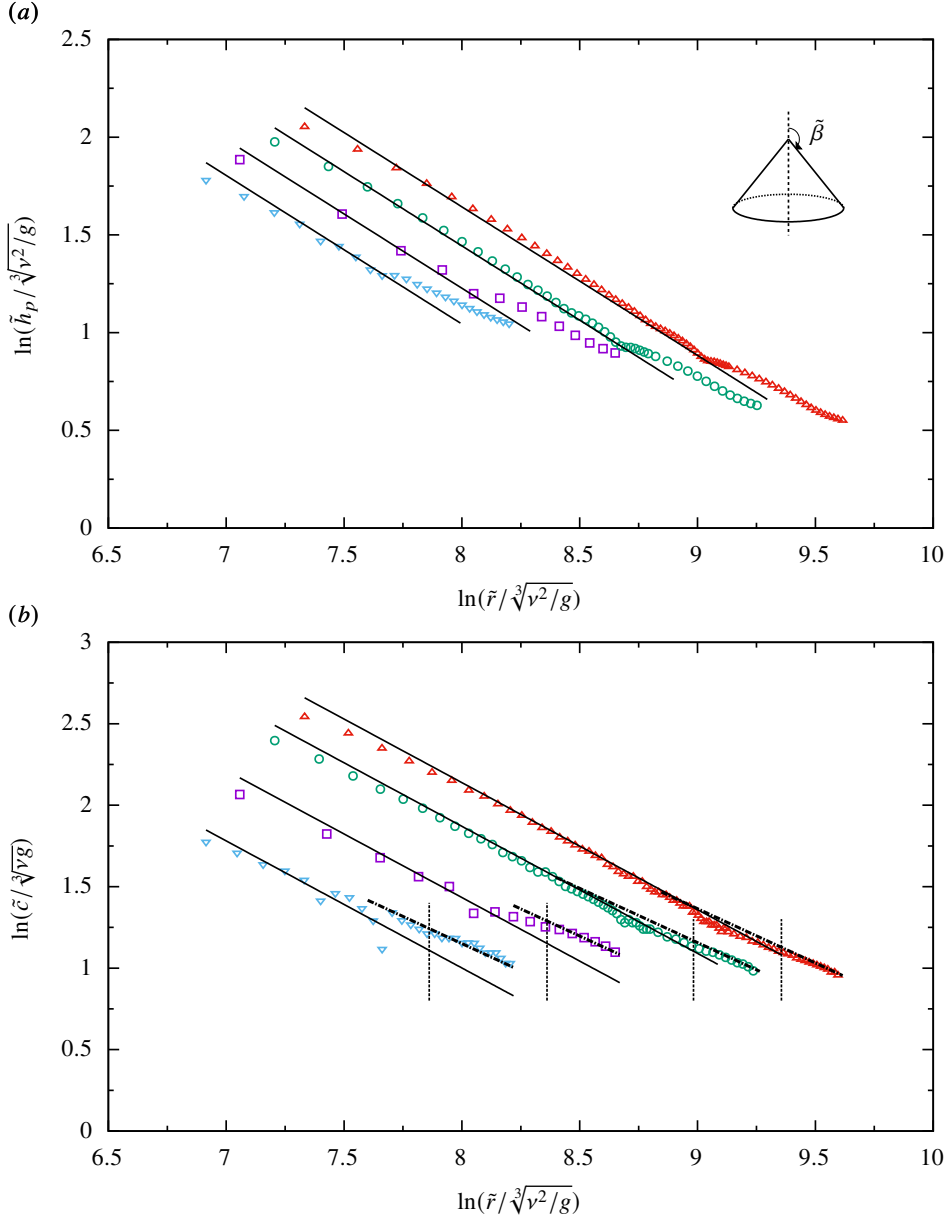


Figure 17: Peak height (a) and phase speed (b) versus radial distance. Symbols: h - q model. Solid lines: Eq. (5.9) and Eq. (5.8). Blue inverted triangles: $\tilde{\beta} = 110^\circ$, $Ka_\perp = 240$, $N_{q\perp} = 8969$, $N_{\omega\perp} = 0.177$; purple squares: $\tilde{\beta} = 120^\circ$, $Ka_\perp = 240$, $N_{q\perp} = 12084$, $N_{\omega\perp} = 0.228$; green circles: $\tilde{\beta} = 140^\circ$, $Ka_\perp = 242$, $N_{q\perp} = 11242$, $N_{\omega\perp} = 0.221$; red triangles: $\tilde{\beta} = 150^\circ$, $Ka_\perp = 242$, $N_{q\perp} = 11242$, $N_{\omega\perp} = 0.221$. Dash-dotted lines in panel (b): Eq. (5.1); vertical dashed lines mark positions where the fundamental frequency amplitude exceeds 90%, see section 5.2. A depiction of $\tilde{\beta}$ is displayed in panel (a).

the right cone (green solid line) and inverted cone (purple solid line). The latter decreases monotonically with \tilde{r} and lies slightly above the relative-growth curves. As expected, for the inverted cone on which the liquid converges towards the apex with film thickening, it is more stringent for the flow to be stable in the sense of absolute growth than relative growth.

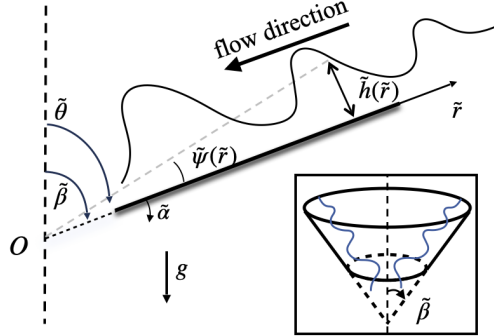


Figure 18: Geometric configuration for liquid film flow along the upper surface of an inverted cone. The bottom of the cone is open to allow the drainage of liquid.

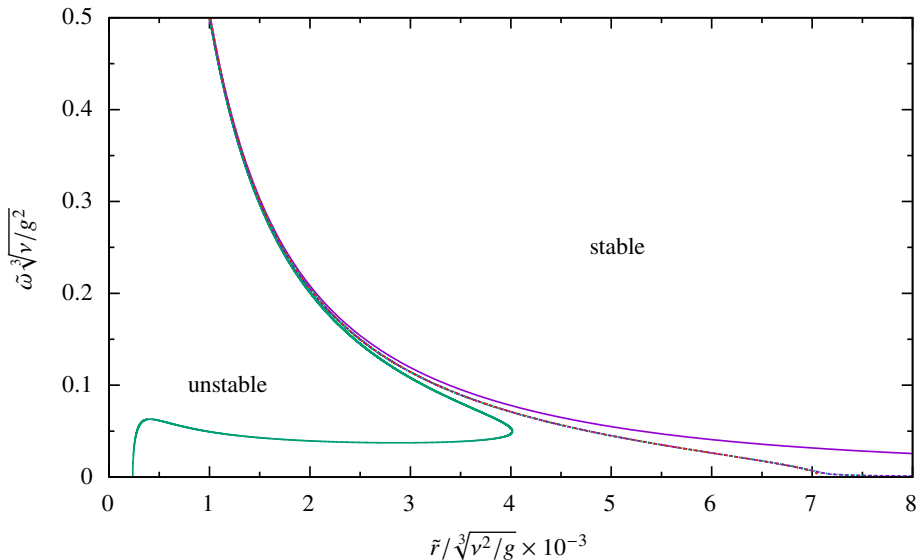


Figure 19: Neutral stability curves for absolute (solid lines) and relative (dashed lines) growth. Green: cone; purple: inverted cone; red: flat plate. The values of $\tilde{\beta}$, Ka_{\perp} , and $N_{q\perp}$ are the same as in figure 3.

The characteristics of large-amplitude surface waves obtained with the h - q model are illustrated in figure 20. Panels (a) and (b) present the instantaneous wave profile and spatio-temporal evolution, respectively. The liquid enters the computational domain at $\tilde{r}_{\text{in}}/\tilde{h}_{\text{out}} = 400$ and leaves at $\tilde{r}_{\text{out}}/\tilde{h}_{\text{out}} = 20$ (\tilde{r}_{out} and \tilde{h}_{out} are related through Eq. (3.5), or its dimensional form, Eq. (1.5)). The wavelength, peak height, and phase speed all increase with decreasing \tilde{r} , mirroring the trends observed in figure 9.

The two situations with supplementary polar angles are further compared quantitatively in figure 21. The purple solid lines represent the right-cone case with $\tilde{\beta} = 135^\circ$. The blue dashed lines denote the inverted-cone case with $\tilde{\beta} = 180^\circ - 135^\circ = 45^\circ$. For both the peak height (a) and phase speed (b) of the surface waves, the two lines almost coincide at large \tilde{r} . The discrepancy at small \tilde{r} is due to the transient effect close to the inlet of the right-cone situation.

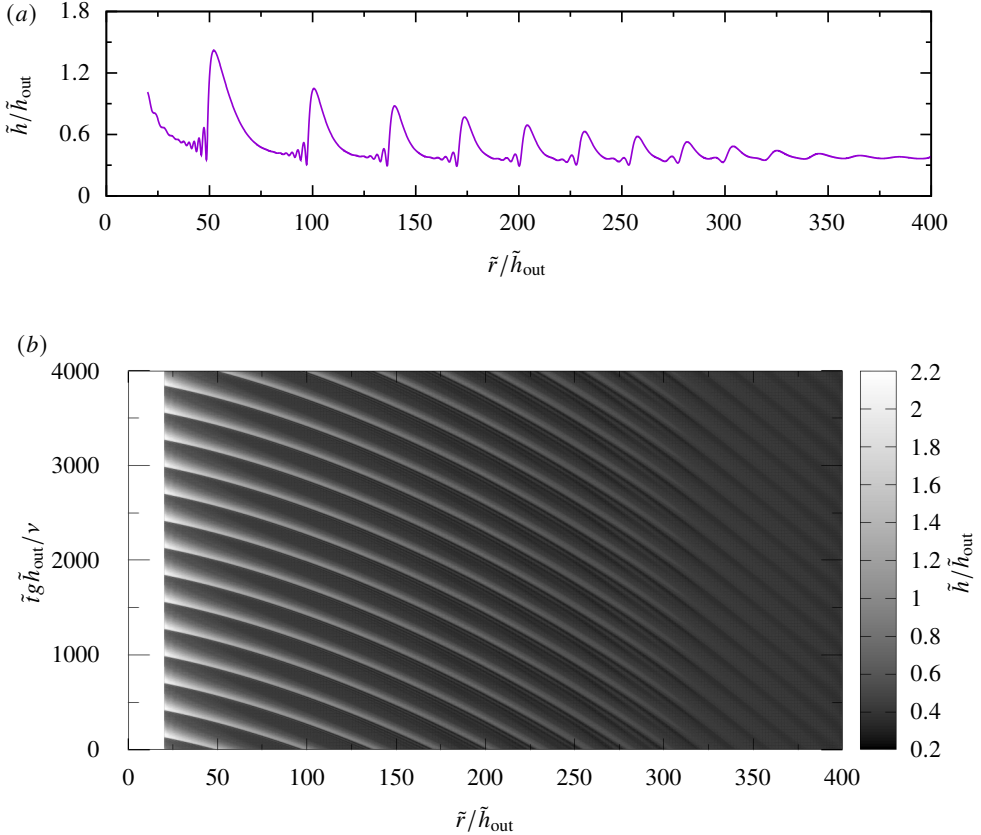


Figure 20: (a) Shape of free surface for liquid film flow on the upper surface of an inverted cone ($\beta = 60^\circ$). (b) Contour map of spatio-temporal wave evolution for the same case. Brightness indicates local film thickness. Liquid properties and disturbance frequency are the same as in figure 9.

The nearly identical behaviors in the fully developed region echoes figure 19: inverting the cone has negligible influence on wave properties provided that the film remains on the upper surface. This feature can be explained by the long-wave nature of the flow field, which means the film thickness, as well as the volumetric flow rate per unit width, changes slowly in the radial direction. As a consequence, the local flow field on either a right cone or an inverted cone resembles the two-dimensional flat-plate case whose parameters are the same as the local values of the conical ones.

That being said, because of inertial effects, the flow field adjust to the local geometry more slowly than the geometry itself changes. Therefore, the properties tend to retain upstream information, especially in the small \tilde{r} region where the divergence/convergence is stronger. This effect can be somewhat observed from figure 21, where the solid lines are slightly above the dashed lines.

An implication of figure 19 is illustrated in figure 22: for an inverted cone, an inlet disturbance may first decay and then grow at smaller \tilde{r} where the flow becomes unstable to the imposed frequency. The inset locates the minimum-amplitude position at $\tilde{r}/\tilde{h}_{\text{out}} \approx 614$, within 6% deviation from the linear-theory stability threshold 650. The free surface around

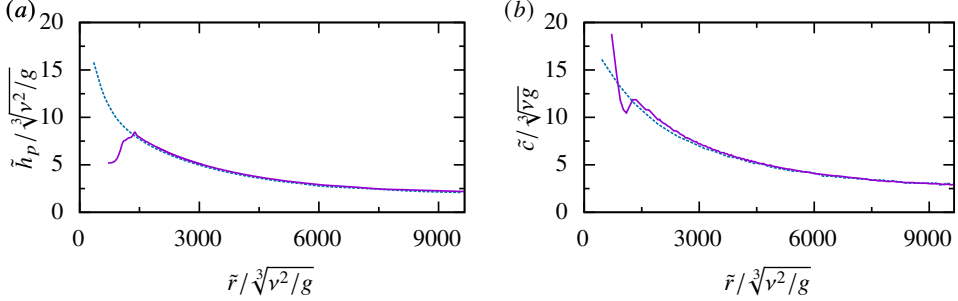


Figure 21: Peak height (a) and phase speed (b) of surface waves on a liquid film along the upper surface of a cone (purple solid lines) and an inverted cone (blue dashed lines); $Ka_\perp = 240$, $N_{\omega\perp} = 0.177$, and $N_{q\perp} = 13954$. The polar angles for the cone and inverted cone are supplementary, with their values of $\tilde{\beta} = 135^\circ$ and 45° , respectively.

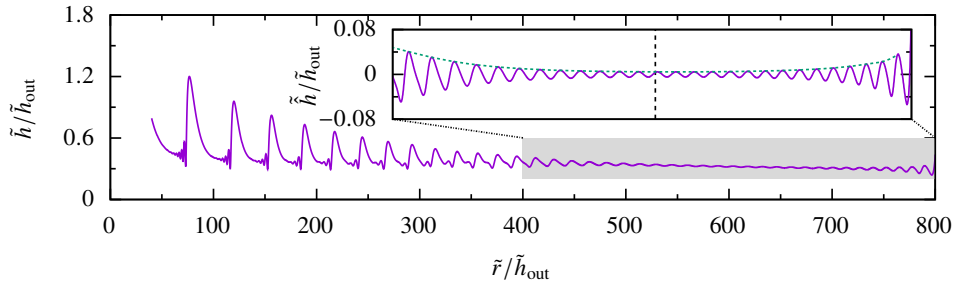


Figure 22: Shape of free surface for liquid film flow on the upper surface of an inverted cone. The disturbance is imposed at $\tilde{r}/\tilde{h}_{\text{out}} = 800$. Liquid properties and disturbance frequency are the same as in figure 9. Inset: \tilde{h} (defined in Eq. (3.10)) as a function of \tilde{r} . The transition position is determined as the position where the wave amplitude is minimum.

this location is nearly flat. A reduction of heat- and mass-transfer rate across the film is expected in this region.

7. Further considerations on the long-wave expansion

7.1. Validity range of the theory

Stemming from the long-wave assumption, both the linear stability analysis and the h - q model are expected to be valid for $\varepsilon = H/L \ll 1$. As a conservative estimate, we set $H/L \lesssim 0.01$. Replacing L with the radial distance \tilde{r} and H with the local film thickness estimated using Eq. (1.5), one obtains an inequality for \tilde{r} , whose solution reads

$$\tilde{r} \gtrsim 100^{3/4} \left(-\frac{3v\tilde{Q}}{2\pi g \sin \tilde{\beta} \cos \tilde{\beta}} \right)^{1/4}. \quad (7.1)$$

For all data shown in the present paper, the minimal radial distance where they are extracted is taken around the threshold predicted by Eq. (7.1). In figures 7(a) and 7(b), these thresholds for \tilde{r} are indicated by vertical dashed lines.

Another assumption that is made during the derivation is the smallness of the Reynolds number, i.e., $Re \sim O(1)$. However, comparisons with DNS (figure 7) and experimental results (figure 8) demonstrate that, the current h - q model works consistently well up to $Re \lesssim 10$; and major wave properties can still be captured at $Re \lesssim 100$. Such good performance

“beyond expectation” has been richly documented for the h - q model families derived from the long-wave expansion in the flat-plate scenario.

7.2. A double- ε expansion strategy

In the Navier-Stokes equations (2.1)-(2.3), there are two ways in which the radial distance \tilde{r} is involved: it may appear alone (e.g., \tilde{r} , \tilde{r}^{-1} , and \tilde{r}^{-2}) or in the denominator of partial derivatives (e.g., $\partial/\partial\tilde{r}$ and $\partial^2/\partial\tilde{r}^2$). Strictly speaking, \tilde{r} in the two scenarios should not be normalized using the same characteristic length: while an individual \tilde{r} reflects the influence of the radial distance itself on the flow, the derivatives of physical quantities with respect to \tilde{r} represent how quickly these quantities vary with \tilde{r} . The length scale across which these variations occur is the local wavelength, yet is irrelevant to \tilde{r} ’s absolute value. Accordingly, an individual \tilde{r} should be normalized by its own scale, whereas \tilde{r} in the bottom of derivatives is more appropriate to be normalized using the wavelength[†]. Based on this consideration, the nondimensionalization and long-wave expansion of the Navier-Stokes equations can be refined as follows.

Let L_1 and L_2 denote the characteristic length scales for the radial distance and wavelength, respectively. Two, instead of one, small parameters can be defined as

$$\varepsilon_1 = \frac{H}{L_1} \ll 1, \quad \text{and} \quad \varepsilon_2 = \frac{H}{L_2} \ll 1. \quad (7.2)$$

Since $|\tilde{\psi}| \approx \tilde{h}/\tilde{r}$, $\tilde{\psi}$ as well as $\tilde{\alpha}$ is of order $O(\varepsilon_1)$. With $u = \tilde{u}/U$ and $v = \tilde{v}/V$, the balance of continuity equation leads to $V/U \sim \varepsilon_2$. Thus, the following scalings are adopted:

$$\tilde{r} = L_1 r, \quad \frac{\partial}{\partial\tilde{r}} = \frac{1}{L_2} \frac{\partial}{\partial r}, \quad \tilde{\alpha} = \varepsilon_1 \alpha, \quad \tilde{u} = U u, \quad \tilde{v} = \varepsilon_2 U v, \quad \tilde{t} = \frac{L_2 t}{U}, \quad \tilde{p} = \rho g H p. \quad (7.3)$$

On substitution, the dimensionless Navier-Stokes equations read

$$\frac{\partial u}{\partial r} + \frac{1}{r} \frac{\partial v}{\partial \alpha} + 2 \frac{\varepsilon_1}{\varepsilon_2} \frac{u}{r} + \varepsilon_1 \frac{v}{r} \cot \beta - \varepsilon_1^2 \frac{v}{r} \alpha \csc^2 \beta = 0, \quad (7.4)$$

$$\begin{aligned} \varepsilon_2 Re \frac{\partial u}{\partial t} + \varepsilon_2 Re u \frac{\partial u}{\partial r} + \varepsilon_2 Re \frac{v}{r} \frac{\partial u}{\partial \alpha} &= -\cos \beta + \varepsilon_1 \alpha \sin \beta + \frac{1}{2} \varepsilon_1^2 \alpha^2 \cos \beta - \varepsilon_2 \frac{\partial p}{\partial r} \\ + \varepsilon_1 \varepsilon_2 \frac{\partial^2 u}{\partial r^2} + \varepsilon_1 \varepsilon_2 \frac{2}{r} \frac{\partial u}{\partial r} + \frac{1}{r^2} \frac{\partial^2 u}{\partial \alpha^2} + \varepsilon_1 \frac{\cot \beta}{r^2} \frac{\partial u}{\partial \alpha} - \varepsilon_1^2 \frac{\alpha \csc^2 \beta}{r^2} \frac{\partial u}{\partial \alpha} &- \varepsilon_1^2 \frac{2}{r^2} - \varepsilon_1 \varepsilon_2 \frac{2}{r^2} \frac{\partial v}{\partial \alpha}, \end{aligned} \quad (7.5)$$

and

$$0 = \sin \beta + \varepsilon_1 \alpha \cos \beta - \frac{1}{r} \frac{\partial p}{\partial \alpha} + \varepsilon_2 \frac{1}{r^2} \frac{\partial^2 v}{\partial \alpha^2} + \varepsilon_1 \frac{2}{r^2} \frac{\partial u}{\partial \alpha}. \quad (7.6)$$

The no-slip boundary condition at the wall is the same as Eq. (2.16). And the kinematic boundary condition at the free surface becomes

$$\frac{\partial h}{\partial t} - \frac{\varepsilon_1}{\varepsilon_2} \frac{h u}{r} + u \frac{\partial h}{\partial r} + v = 0. \quad (7.7)$$

[†] An exception is the situation in which the independent variable \tilde{r} appears in the numerator of the derivative, as the length scale for the change of \tilde{r} is itself (L_1), instead of the wavelength L_2 . For example, as is evident, $\partial\tilde{r}/\partial\tilde{r}$ should have the order $L_1/L_1 \sim O(1)$ instead of $L_1/L_2 \sim O(\varepsilon_2/\varepsilon_1)$. Thus, care should be taken when dealing with terms such as $\partial\tilde{\psi}/\partial\tilde{r} \approx -\partial(\tilde{h}/\tilde{r})/\partial\tilde{r}$, in which case the normalization should be performed after expansion, i.e., after \tilde{r} is removed from the numerator of the partial derivative.

The tangential and normal stress balances at the free surface are given by

$$\frac{1}{r} \frac{\partial u}{\partial \alpha} = 2 \left(\varepsilon_1 \frac{\partial u}{\partial r} - \varepsilon_1 \frac{u}{r} - \varepsilon_2 \frac{1}{r} \frac{\partial v}{\partial \alpha} \right) \left(-\varepsilon_2 \frac{\partial h}{\partial r} + \varepsilon_1 \frac{h}{r} \right) - \varepsilon_1 \varepsilon_2 \left(\frac{\partial v}{\partial r} + \frac{v}{r} \right) \quad (7.8)$$

and

$$-p + 2 \left(\varepsilon_2 \frac{1}{r} \frac{\partial v}{\partial \alpha} + \varepsilon_1 \frac{u}{r} \right) = \left(\frac{\varepsilon_2}{Bo} \right) C, \quad (7.9)$$

respectively, where the curvature C is

$$C = \frac{\varepsilon_1}{\varepsilon_2} \frac{1}{r} \cot \beta + \frac{\varepsilon_1^2}{\varepsilon_2 r^2} \frac{h}{r^2} \cot^2 \beta + \varepsilon_1 \frac{1}{r} \frac{\partial h}{\partial r} + \varepsilon_2 \frac{\partial^2 h}{\partial r^2}. \quad (7.10)$$

It is worthwhile to note that, when $\varepsilon_1 \sim \varepsilon_2 \sim \varepsilon$, which correspond to regions not too far from the cone apex, Eqs. (7.4)-(7.10) reduce to Eqs. (2.13)-(2.20). Whereas for positions at which the radial distance is much larger than the local wavelength, i.e., $\varepsilon_1 \ll \varepsilon_2$, the effect of ε_1 terms in Eqs. (7.4)-(7.10) diminishes or even vanishes in the present second-order framework. In such a scenario, Eqs. (2.13)-(2.20) actually contain extra high-order (higher than second order) ε_1 terms, representing a more conservative approximation.

With the above preparations, we are able to examine the impact of different terms in the expression of curvature, Eq. (7.10). In this equation, the first term is the lateral curvature whose order is $O(\varepsilon_1/\varepsilon_2)$. The last three terms represent the contribution of the streamwise curvature, with their orders of magnitude being $O(\varepsilon_1^2/\varepsilon_2)$, $O(\varepsilon_1)$, and $O(\varepsilon_2)$, respectively. If $\varepsilon_1 \sim \varepsilon_2$, the lateral curvature is dominant. However, as \tilde{r} increases (thus ε_1 decreases), its influence weakens, rendering the last term of the streamwise curvature pronounced. In other words, the present double- ε expansion approach reveals that, the lateral curvature is a dominant quantity only in the region close to the apex. It degrades to higher orders as \tilde{r} increases. Physically speaking, this behavior reflects the vanishing effect of cone surface curvature far from the apex.

8. Summary and conclusions

In this study, the linear and nonlinear wave dynamics of axisymmetric thin liquid film flow on a conical surface are systematically investigated. The linear stability result of Zollars & Krantz (1980) is improved by including the streamwise curvature of the free surface, which is found to have a non-negligible stabilizing effect. A second-order h - q model is derived using the weighted residual integral boundary-layer approach. The model is shown to predict the wave dynamics with good accuracy and efficiency at moderate Reynolds numbers.

Unlike the liquid film flow on an inclined flat plate which is irrelevant to the streamwise coordinate, the characteristics of surface waves on a cone exhibit strong dependence on the radial distance \tilde{r} from the apex. Together with the progressively thinning of the film due to the divergent geometry, a transition from solitary to sinusoidal waves is observed as \tilde{r} increases. The transition position is found to coincide with the stability threshold in the sense of relative growth. The peak height and phase speed of the surface waves also decrease with \tilde{r} . In the solitary-wave region, these quantities can be predicted by empirical correlations similar to those proposed by Nosoko *et al.* (1996); whereas the phase speed of the sinusoidal waves are well described by the linear theory.

Additionally, results are compared with liquid film flow on the upper surface of an inverted cone whose half-apex angle is supplementary to that of the right cone. Differences in most linear and nonlinear wave characteristics are small, indicating negligible inertial influence on wave evolution. This observation implies the applicability of quantitative flat-plate results

in the conical scenarios, provided the local film thickness, flow rate, and Reynolds number Re_ℓ are substituted. Because Re_ℓ varies continuously along the conical surface, a single experiment or numerical simulation yields a data set spanning a wide range of Re_ℓ . This data can then be used to efficiently develop and validate correlations for the flat-plate situation.

In industrial applications, liquid film flow is often accompanied by heat and mass transfer across the film (see, e.g., Tanguy *et al.* 2015; Zhou & Prosperetti 2020b). These processes are jointly influenced by film thickness and surface-wave dynamics. In general, higher heat- and mass-transfer efficiency is favored by thinner films and more pronounced solitary waves, yet the two compete on a conical surface. In film coating operations (e.g. Quéré 1999; Benilov & Zubkov 2008; Molefe *et al.* 2024; Pino *et al.* 2024), adjustment of film thickness is sometimes required (Lacanette *et al.* 2006). Therefore, research on optimization and control strategies (see, e.g. Aniszewski *et al.* 2020; Mendez *et al.* 2021; Barreiro-Villaverde *et al.* 2024) for conical liquid film flow is needed in the future. Coating flows are also seen in natural environments, such as in the formation of karst landscapes. The stability of such flows and the associated surface waves are believed to play a crucial role in shaping speleothem morphology within limestone caves (Camporeale & Ridolfi 2012; Ledda *et al.* 2021, 2022). These speleothems, particularly stalagmites and stalactites, often exhibit elongated conical shapes, whose formation involves low-Reynolds-number flows (Short *et al.* 2005). Therefore, the methods and discussions proposed in the current work are potentially useful in hydrodynamic studies related to stalagmite/stalactite growth.

Compared with stationary cones, rotating geometries exhibit even richer phenomena (see, e.g., Kim & Kim 2024; Stafford *et al.* 2025) and have broad industrial applications (e.g., Duruk *et al.* 2023; Shepherd *et al.* 2024). Linear stability, nonlinear wave evolution, and quantitative wave characteristics on rotating cones warrant further investigation.

The current work focuses on the response of liquid films under axisymmetric disturbances. In practice, transition to fully three-dimensional flows may occur due to lateral disturbances. Future work is needed to extend the present analysis and $h\text{-}q$ model to fully three-dimensional versions. In that case, the superiority of low-dimensional models over 3D DNS simulations would be more significant.

Acknowledgements. The authors thank Prof. Andrea Prosperetti for insightful discussions during the preparation of this work.

Funding. The authors acknowledge the support of the National Natural Science Foundation of China (12202441, 12572298) and the Fundamental Research Funds for the Central Universities.

Declaration of interests. The authors report no conflict of interest.

Appendix A. Derivation of the curvature at the free surface

The position of the free surface can be expressed by the equation $\tilde{\alpha} - \tilde{\psi}(\tilde{r}, \tilde{t}) \equiv 0$. Accordingly, the unit normal vector is given by

$$\tilde{\mathbf{n}} = \frac{\nabla(\tilde{\alpha} - \tilde{\psi})}{\|\nabla(\tilde{\alpha} - \tilde{\psi})\|} = \frac{1}{\sqrt{1 + (\tilde{r}\partial_{\tilde{r}}\tilde{\psi})^2}} [-\tilde{r}\partial_{\tilde{r}}\tilde{\psi}, 1, 0]^T. \quad (\text{A } 1)$$

The curvature is calculated as

$$\tilde{C} = \nabla \cdot \tilde{\mathbf{n}} = \frac{1}{\tilde{r}^2} \frac{\partial}{\partial \tilde{r}} \left[\tilde{r}^2 \left(-\frac{\tilde{r}\partial_{\tilde{r}}\tilde{\psi}}{\sqrt{1 + (\tilde{r}\partial_{\tilde{r}}\tilde{\psi})^2}} \right) \right] + \frac{1}{\tilde{r} \sin \tilde{\theta}} \frac{\partial}{\partial \tilde{\theta}} \left(\frac{\sin \tilde{\theta}}{\sqrt{1 + (\tilde{r}\partial_{\tilde{r}}\tilde{\psi})^2}} \right). \quad (\text{A } 2)$$

On substitution of $\tilde{\theta} = \tilde{\beta} + \tilde{\psi}$, Eq. (A 2) yields

$$\tilde{C} = \frac{1}{\tilde{r}\sqrt{1 + (\tilde{r}\partial_{\tilde{r}}\tilde{\psi})^2}} \left[\cot(\tilde{\beta} + \tilde{\psi}) - 2\tilde{r}\partial_{\tilde{r}}\tilde{\psi} - \frac{\tilde{r}(\partial_{\tilde{r}}\tilde{\psi} + \tilde{r}\partial_{\tilde{r}}^2\tilde{\psi})}{1 + (\tilde{r}\partial_{\tilde{r}}\tilde{\psi})^2} \right], \quad (\text{A 3})$$

whose dimensionless form reads

$$C = \frac{1}{r\sqrt{1 + (\varepsilon r\partial_r\psi)^2}} \left[\cot(\beta + \varepsilon\psi) - 2\varepsilon r\partial_r\psi - \frac{r(\varepsilon\partial_r\psi + \varepsilon r\partial_r^2\psi)}{1 + (\varepsilon r\partial_r\psi)^2} \right]. \quad (\text{A 4})$$

On substitution of $\psi \approx -h/r$ into Eq. (A 4), applying Taylor expansions, and retaining terms up to $O(\varepsilon)$, one obtains Eq. (2.20).

Appendix B. Some results in the linear stability analysis

The results of the asymptotic expansions for u , v , and p shown in Eq. (3.1) are presented here for reader's convenience ($v^{(2)}$ and $p^{(2)}$ are not listed as they are not used in the derivation):

$$v^{(0)} = -\frac{2\alpha^3 r^2 \cos \beta}{3} - \frac{\alpha^2 r^2 \cos \beta}{2} \frac{\partial h}{\partial r} - \frac{3\alpha^2 r h \cos \beta}{2}, \quad (\text{B 1})$$

$$p^{(0)} = \alpha r \sin \beta + h \sin \beta - \left(\frac{\varepsilon}{Bo} \right) \frac{\cos \beta}{r \sin \beta}, \quad (\text{B 2})$$

$$\begin{aligned} u^{(1)} = & -\frac{Re\alpha^6 r^5 \cos^2 \beta}{180} - \frac{Re\alpha^5 r^4 h \cos^2 \beta}{30} + \frac{Re\alpha^4 r^4 h \cos^2 \beta}{24} \frac{\partial h}{\partial r} - \frac{Re\alpha^4 r^3 h^2 \cos^2 \beta}{24} \\ & + \frac{Re\alpha^3 r^3 h^2 \cos^2 \beta}{6} \frac{\partial h}{\partial r} + \frac{Re\alpha^3 r^2 h^3 \cos^2 \beta}{18} - \frac{Re\alpha r h^4 \cos^2 \beta}{3} \frac{\partial h}{\partial r} - \frac{Re\alpha h^5 \cos^2 \beta}{5} \\ & - \frac{\alpha^3 r^2 \cos^2 \beta}{6 \sin \beta} + \frac{\alpha^2 r^2 \sin \beta}{2} \frac{\partial h}{\partial r} - \frac{\alpha^2 r h \cos^2 \beta}{2 \sin \beta} + \alpha r h \sin \beta \frac{\partial}{\partial r} h - \frac{\alpha h^2 \cos^2 \beta}{2 \sin \beta} \\ & + \left(\frac{\varepsilon}{Bo} \right) \left(\frac{\alpha^2 \cos \beta}{2 \sin \beta} + \frac{\alpha h \cos \beta}{r \sin \beta} \right), \end{aligned} \quad (\text{B 3})$$

$$\begin{aligned}
v^{(1)} = & \frac{Re\alpha^7 r^5 \cos^2 \beta}{180} + \frac{Re\alpha^6 r^5 \cos^2 \beta}{180} \frac{\partial h}{\partial r} + \frac{Re\alpha^6 r^4 h \cos^2 \beta}{30} - \frac{Re\alpha^5 r^5 h \cos^2 \beta}{120} \frac{\partial^2 h}{\partial r^2} \\
& - \frac{Re\alpha^5 r^5 \cos^2 \beta}{120} \left(\frac{\partial h}{\partial r} \right)^2 - \frac{Re\alpha^5 r^4 h \cos^2 \beta}{30} \frac{\partial h}{\partial r} + \frac{Re\alpha^5 r^3 h^2 \cos^2 \beta}{24} \\
& - \frac{Re\alpha^4 r^4 h^2 \cos^2 \beta}{24} \frac{\partial^2 h}{\partial r^2} - \frac{Re\alpha^4 r^4 h \cos^2 \beta}{12} \left(\frac{\partial h}{\partial r} \right)^2 - \frac{Re\alpha^4 r^3 h^2 \cos^2 \beta}{4} \frac{\partial h}{\partial r} \\
& - \frac{Re\alpha^4 r^2 h^3 \cos^2 \beta}{18} + \frac{Re\alpha^2 r^2 h^4 \cos^2 \beta}{6} \frac{\partial^2 h}{\partial r^2} + \frac{2Re\alpha^2 r^2 h^3 \cos^2 \beta}{3} \left(\frac{\partial h}{\partial r} \right)^2 \\
& + Re\alpha^2 r h^4 \cos^2 \beta \frac{\partial h}{\partial r} + \frac{Re\alpha^2 h^5 \cos^2 \beta}{5} + \frac{\alpha^4 r^2 \cos^2 \beta}{3 \sin \beta} - \frac{\alpha^3 r^3 \sin \beta}{6} \frac{\partial^2 h}{\partial r^2} \\
& - \frac{2\alpha^3 r^2 \sin \beta}{3} \frac{\partial h}{\partial r} + \frac{\alpha^3 r^2 \cos^2 \beta}{3 \sin \beta} \frac{\partial h}{\partial r} + \frac{\alpha^3 r h \cos^2 \beta}{\sin \beta} - \frac{\alpha^2 r^2 h \sin \beta}{2} \frac{\partial^2 h}{\partial r^2} \\
& - \frac{\alpha^2 r^2 \sin \beta}{2} \left(\frac{\partial h}{\partial r} \right)^2 - \frac{3\alpha^2 r h \sin \beta}{2} \frac{\partial h}{\partial r} + \frac{\alpha^2 r h \cos^2 \beta}{2 \sin \beta} \frac{\partial h}{\partial r} + \frac{\alpha^2 h^2 \cos^2 \beta}{2 \sin \beta} \\
& - \left(\frac{\varepsilon}{Bo} \right) \left(\frac{\alpha^3 \cos \beta}{3 \sin \beta} + \frac{\alpha^2 \cos \beta}{2 \sin \beta} \frac{\partial h}{\partial r} + \frac{\alpha^2 h \cos \beta}{2r \sin \beta} \right), \tag{B 4}
\end{aligned}$$

$$\begin{aligned}
p^{(1)} = & - \frac{\alpha^2 r \cos \beta}{2} - \alpha r \cos \beta \frac{\partial}{\partial r} h - \alpha h \cos \beta + h \cos \beta \frac{\partial}{\partial r} h + \frac{h^2 \cos \beta}{2r} \\
& - \left(\frac{\varepsilon}{Bo} \right) \left(\frac{\partial^2 h}{\partial r^2} + \frac{1}{r} \frac{\partial h}{\partial r} + \frac{h \cos^2 \beta}{r^2 \sin^2 \beta} \right), \tag{B 5}
\end{aligned}$$

$$\begin{aligned}
u^{(2)} = & \frac{Re^2 \alpha^{10} r^8 \cos^3 \beta}{10800} + \frac{Re^2 \alpha^9 r^7 h \cos^3 \beta}{1080} + \frac{Re^2 \alpha^8 r^8 h \cos^3 \beta}{4480} \frac{\partial^2 h}{\partial r^2} + \frac{Re^2 \alpha^8 r^8 \cos^3 \beta}{4480} \left(\frac{\partial h}{\partial r} \right)^2 \\
& - \frac{Re^2 \alpha^8 r^7 h \cos^3 \beta}{1440} \frac{\partial h}{\partial r} + \frac{17Re^2 \alpha^8 r^6 h^2 \cos^3 \beta}{5760} + \frac{Re^2 \alpha^7 r^7 h^2 \cos^3 \beta}{560} \frac{\partial^2 h}{\partial r^2} + \frac{Re^2 \alpha^7 r^7 h \cos^3 \beta}{560} \left(\frac{\partial h}{\partial r} \right)^2 \\
& - \frac{Re^2 \alpha^7 r^6 h^2 \cos^3 \beta}{180} \frac{\partial h}{\partial r} + \frac{Re^2 \alpha^7 r^5 h^3 \cos^3 \beta}{720} + \frac{Re^2 \alpha^6 r^6 h^3 \cos^3 \beta}{180} \frac{\partial^2 h}{\partial r^2} + \frac{7Re^2 \alpha^6 r^6 h^2 \cos^3 \beta}{720} \left(\frac{\partial h}{\partial r} \right)^2 \\
& - \frac{Re^2 \alpha^6 r^5 h^3 \cos^3 \beta}{135} \frac{\partial h}{\partial r} - \frac{13Re^2 \alpha^6 r^4 h^4 \cos^3 \beta}{2160} + \frac{Re^2 \alpha^5 r^5 h^4 \cos^3 \beta}{120} \frac{\partial^2 h}{\partial r^2} + \frac{Re^2 \alpha^5 r^5 h^3 \cos^3 \beta}{30} \left(\frac{\partial h}{\partial r} \right)^2 \\
& + \frac{Re^2 \alpha^5 r^4 h^4 \cos^3 \beta}{30} \frac{\partial h}{\partial r} + \frac{Re^2 \alpha^5 r^3 h^5 \cos^3 \beta}{150} - \frac{Re^2 \alpha^4 r^4 h^5 \cos^3 \beta}{72} \frac{\partial^2 h}{\partial r^2} - \frac{5Re^2 \alpha^4 r^4 h^4 \cos^3 \beta}{72} \left(\frac{\partial h}{\partial r} \right)^2 \\
& - \frac{Re^2 \alpha^4 r^3 h^5 \cos^3 \beta}{45} \frac{\partial h}{\partial r} + \frac{Re^2 \alpha^4 r^2 h^6 \cos^3 \beta}{40} - \frac{7Re^2 \alpha^3 r^3 h^6 \cos^3 \beta}{90} \frac{\partial^2 h}{\partial r^2} - \frac{7Re^2 \alpha^3 r^3 h^5 \cos^3 \beta}{15} \left(\frac{\partial h}{\partial r} \right)^2 \\
& - \frac{56Re^2 \alpha^3 r^2 h^6 \cos^3 \beta}{135} \frac{\partial h}{\partial r} - \frac{Re^2 \alpha^3 r h^7 \cos^3 \beta}{27} + \frac{10Re^2 \alpha r h^8 \cos^3 \beta}{63} \frac{\partial^2 h}{\partial r^2} + \frac{316Re^2 \alpha r h^7 \cos^3 \beta}{315} \left(\frac{\partial h}{\partial r} \right)^2 \\
& + \frac{44Re^2 \alpha h^8 \cos^3 \beta}{45} \frac{\partial h}{\partial r} + \frac{4Re^2 \alpha h^9 \cos^3 \beta}{27r} + \frac{11Re\alpha^7 r^5 \cos^3 \beta}{1260 \sin \beta} + \frac{Re\alpha^6 r^6 \sin \beta \cos \beta}{360} \frac{\partial^2 h}{\partial r^2} \\
& - \frac{Re\alpha^6 r^5 \sin \beta \cos \beta}{90} \frac{\partial h}{\partial r} + \frac{Re\alpha^6 r^5 \cos^3 \beta}{180 \sin \beta} \frac{\partial h}{\partial r} + \frac{Re\alpha^6 r^4 h \cos^3 \beta}{18 \sin \beta} + \frac{Re\alpha^5 r^5 h \sin \beta \cos \beta}{60} \frac{\partial^2 h}{\partial r^2} \\
& - \frac{Re\alpha^5 r^4 h \sin \beta \cos \beta}{15} \frac{\partial h}{\partial r} - \frac{Re\alpha^5 r^4 h \cos^3 \beta}{60 \sin \beta} \frac{\partial h}{\partial r} + \frac{Re\alpha^5 r^3 h^2 \cos^3 \beta}{10 \sin \beta} + \frac{Re\alpha^4 r^4 h^2 \sin \beta \cos \beta}{12} \frac{\partial^2 h}{\partial r^2} \\
& + \frac{Re\alpha^4 r^4 h \sin \beta \cos \beta}{6} \left(\frac{\partial h}{\partial r} \right)^2 - \frac{Re\alpha^4 r^3 h^2 \sin \beta \cos \beta}{24} \frac{\partial h}{\partial r} - \frac{7Re\alpha^4 r^3 h^2 \cos^3 \beta}{48 \sin \beta} \frac{\partial h}{\partial r} - \frac{Re\alpha^4 r^2 h^3 \sin \beta \cos \beta}{72} \\
& + \frac{5Re\alpha^4 r^2 h^3 \cos^3 \beta}{144 \sin \beta} + \frac{2Re\alpha^3 r^3 h^3 \sin \beta \cos \beta}{9} \frac{\partial^2 h}{\partial r^2} + \frac{2Re\alpha^3 r^3 h^2 \sin \beta \cos \beta}{3} \left(\frac{\partial h}{\partial r} \right)^2 + \frac{5Re\alpha^3 r^2 h^2 \sin \beta \cos \beta}{18} \frac{\partial h}{\partial r} \\
& - \frac{2Re\alpha^3 r^2 h^3 \cos^3 \beta}{9 \sin \beta} \frac{\partial h}{\partial r} - \frac{Re\alpha^3 r h^4 \sin \beta \cos \beta}{18} + \frac{Re\alpha^2 r h^4 \cos^3 \beta}{6 \sin \beta} \frac{\partial h}{\partial r} + \frac{Re\alpha^2 h^5 \cos^3 \beta}{10 \sin \beta} \\
& - \frac{2Re\alpha^2 h^5 \sin \beta \cos \beta}{5} \frac{\partial^2 h}{\partial r^2} - \frac{4Re\alpha^2 h^4 \sin \beta \cos \beta}{3} \left(\frac{\partial h}{\partial r} \right)^2 - \frac{11Re\alpha h^5 \sin \beta \cos \beta}{15} \frac{\partial h}{\partial r} + \frac{8Re\alpha h^5 \cos^3 \beta}{15 \sin \beta} \frac{\partial h}{\partial r} \\
& + \frac{Re\alpha h^6 \sin \beta \cos \beta}{9r} + \frac{Re\alpha h^6 \cos^3 \beta}{9r \sin \beta} - \frac{7\alpha^4 r^2 \cos \beta}{12} + \frac{\alpha^4 r^2 \cos^3 \beta}{24 \sin^2 \beta} + \frac{\alpha^4 r^2 \cos \beta}{12 \sin^2 \beta} - \frac{\alpha^3 r^3 \cos \beta}{3} \frac{\partial^2 h}{\partial r^2} - \frac{3\alpha^3 r^2 \cos \beta}{2} \frac{\partial h}{\partial r} \\
& - \alpha^3 r h \cos \beta + \frac{\alpha^3 r h \cos^3 \beta}{6 \sin^2 \beta} + \frac{\alpha^3 r h \cos \beta}{6 \sin^2 \beta} + \frac{\alpha^2 r^2 h \cos \beta}{2} \frac{\partial^2 h}{\partial r^2} + \frac{\alpha^2 r^2 \cos \beta}{2} \left(\frac{\partial h}{\partial r} \right)^2 - \frac{\alpha^2 h^2 \cos \beta}{4} + \frac{\alpha^2 h^2 \cos^3 \beta}{4 \sin^2 \beta} \\
& + \frac{5\alpha r h^2 \cos \beta}{2} \frac{\partial^2 h}{\partial r^2} + 5\alpha r h \cos \beta \left(\frac{\partial h}{\partial r} \right)^2 + \frac{7\alpha h^2 \cos \beta}{2} \frac{\partial h}{\partial r} - \frac{3\alpha h^3 \cos \beta}{2r} + \frac{\alpha h^3 \cos^3 \beta}{6r \sin^2 \beta} - \frac{\alpha h^3 \cos \beta}{6r \sin^2 \beta} \\
& + \left(\frac{\varepsilon}{Bo} \right) \left(- \frac{Re\alpha^6 r^3 \cos^2 \beta}{60 \sin \beta} - \frac{Re\alpha^5 r^2 h \cos^2 \beta}{10 \sin \beta} + \frac{Re\alpha^4 r^2 h \cos^2 \beta}{12 \sin \beta} \frac{\partial h}{\partial r} - \frac{Re\alpha^4 r h^2 \cos^2 \beta}{6 \sin \beta} + \frac{Re\alpha^3 r h^2 \cos^2 \beta}{3 \sin \beta} \frac{\partial h}{\partial r} \right. \\
& \left. - \frac{2Re\alpha h^4 \cos^2 \beta}{3r \sin \beta} \frac{\partial h}{\partial r} - \frac{4Re\alpha h^5 \cos^2 \beta}{15r^2 \sin \beta} - \frac{\alpha^3 \cos^2 \beta}{6 \sin^2 \beta} - \frac{\alpha^2 r^2 \partial^3 h}{2} - \frac{\alpha^2 r \partial^2 h}{2} + \frac{\alpha^2 \partial h}{2} - \frac{\alpha^2 \cos^2 \beta}{2 \sin^2 \beta} \frac{\partial h}{\partial r} \right. \\
& \left. + \frac{\alpha^2 h \cos^2 \beta}{2r \sin^2 \beta} - \alpha r h \frac{\partial^3 h}{\partial r^3} - \alpha h \frac{\partial^2 h}{\partial r^2} + \frac{\alpha h \partial h}{r} - \frac{\alpha h \cos^2 \beta}{r \sin^2 \beta} \frac{\partial h}{\partial r} + \frac{3\alpha h^2 \cos^2 \beta}{2r^2 \sin^2 \beta} \right). \tag{B 6}
\end{aligned}$$

The Benney-type equation, Eq. (3.3), can be written as

$$\frac{\partial h}{\partial t} = - \frac{1}{r \sin(\beta - \varepsilon h/r)} \frac{\partial}{\partial r} \left(q^{(0)} + \varepsilon q^{(1)} + \varepsilon^2 q^{(2)} \right), \tag{B 7}$$

where

$$q^{(0)} = \int_{\psi}^0 r^2 u^{(0)} \sin \beta d\alpha = -\frac{1}{3} r h^3 \sin \beta \cos \beta, \tag{B 8}$$

$$\begin{aligned}
q^{(1)} &= \int_{\psi}^0 (\alpha r^2 u^{(0)} \cos \beta + r^2 u^{(1)} \sin \beta) d\alpha \\
&= \frac{2Reh^6 \sin \beta \cos^2 \beta}{15} \left(\frac{13h}{21} + r \frac{\partial h}{\partial r} \right) - \frac{rh^3 \sin^2 \beta}{3} \frac{\partial h}{\partial r} + \frac{h^4 \cos^2 \beta}{3} - \left(\frac{\varepsilon}{Bo} \right) \frac{h^3 \cos \beta}{3r},
\end{aligned} \tag{B 9}$$

and

$$\begin{aligned}
q^{(2)} &= \int_{\psi}^0 \left(-\frac{\alpha^2 r^2 u^{(0)} \sin \beta}{2} + \alpha r^2 u^{(1)} \cos \beta + r^2 u^{(2)} \sin \beta \right) d\alpha \\
&= -\frac{4Re^2 rh^{10} \sin \beta \cos^3 \beta}{63} \frac{\partial^2 h}{\partial r^2} - \frac{127Re^2 rh^9 \sin \beta \cos^3 \beta}{315} \left(\frac{\partial h}{\partial r} \right)^2 - \frac{13h^5 \cos^3 \beta}{120r \sin \beta} \\
&\quad - \frac{5608Re^2 h^{10} \sin \beta \cos^3 \beta}{14175} \frac{\partial h}{\partial r} - \frac{9623Re^2 h^{11} \sin \beta \cos^3 \beta}{155925r} - \frac{7Reh^8 \cos^3 \beta}{90r} \\
&\quad + \frac{10Rerh^7 \sin^2 \beta \cos \beta}{63} \frac{\partial^2 h}{\partial r^2} + \frac{8Rerh^6 \sin^2 \beta \cos \beta}{15} \left(\frac{\partial h}{\partial r} \right)^2 + \frac{7h^5 \sin \beta \cos \beta}{8r} \\
&\quad - \frac{67Reh^7 \cos^3 \beta}{252} \frac{\partial h}{\partial r} - \frac{2Reh^8 \sin^2 \beta \cos \beta}{45r} - rh^4 \sin \beta \cos \beta \frac{\partial^2 h}{\partial r^2} \\
&\quad - \frac{7rh^3 \sin \beta \cos \beta}{3} \left(\frac{\partial h}{\partial r} \right)^2 - \frac{7h^4 \sin \beta \cos \beta}{6} \frac{\partial h}{\partial r} + \frac{94Reh^7 \sin^2 \beta \cos \beta}{315} \frac{\partial h}{\partial r} \\
&\quad + \frac{7h^5 \cos \beta}{120r \sin \beta} + \left(\frac{\varepsilon}{Bo} \right) \left(\frac{4Reh^6 \cos^2 \beta}{15r} \frac{\partial h}{\partial r} + \frac{4Reh^7 \cos^2 \beta}{35r^2} + \frac{rh^3 \sin \beta}{3} \frac{\partial^3 h}{\partial r^3} \right. \\
&\quad \left. + \frac{h^3 \sin \beta}{3} \frac{\partial^2 h}{\partial r^2} - \frac{h^3 \sin \beta}{3r} \frac{\partial h}{\partial r} + \frac{h^3 \cos^2 \beta}{3r \sin \beta} \frac{\partial h}{\partial r} - \frac{h^4 \cos^2 \beta}{3r^2 \sin \beta} \right).
\end{aligned} \tag{B 10}$$

The coefficients S_0 - S_4 in the linearized equation, Eq. (3.11), are

$$\begin{aligned}
S_0 &= -\frac{K^2 q_s^{2/3} \cos \beta}{3r^{5/3}} + \varepsilon \left[-\frac{148Req_s^2}{35r^4 \sin^2 \beta} + \frac{q_s}{3r^3 \cos \beta} + \frac{3q_s \cos \beta}{r^3 \sin^2 \beta} + \left(\frac{\varepsilon}{Bo} \right) \frac{5K^2 q_s^{2/3}}{9r^{11/3} \tan \beta} \right] \\
&\quad + \varepsilon^2 \left[-\frac{1486862KRe^2 q_s^{10/3}}{363825r^{19/3} \sin^3 \beta} + \frac{356KReq_s^{7/3}}{189r^{16/3} \sin \beta \cos \beta} - \frac{1093KReq_s^{7/3} \cos \beta}{90r^{16/3} \sin^3 \beta} \right. \\
&\quad \left. + \frac{14Kq_s^{4/3} \sin \beta}{27r^{13/3} \cos^2 \beta} + \frac{4229Kq_s^{4/3}}{216r^{13/3} \sin \beta} + \frac{1781Kq_s^{4/3} \cos^2 \beta}{360r^{13/3} \sin^3 \beta} + \frac{49Kq_s^{4/3}}{40r^{13/3} \sin^3 \beta} \right. \\
&\quad \left. - \left(\frac{\varepsilon}{Bo} \right) \left(\frac{128Req_s^2}{35r^6 \sin^3 \beta} + \frac{34q_s}{9r^5 \sin \beta \cos \beta} + \frac{15q_s \cos \beta}{r^5 \sin^3 \beta} \right) - \left(\frac{\varepsilon}{Bo} \right)^2 \frac{11K^2 q_s^{2/3} \cos \beta}{27r^{17/3} \sin^2 \beta} \right],
\end{aligned} \tag{B 11}$$

$$\begin{aligned}
S_1 = & -\frac{K^2 q_s^{2/3} \cos \beta}{r^{2/3}} + \varepsilon \left[\frac{32 R e q_s^2}{35 r^3 \sin^2 \beta} - \frac{q_s}{3 r^2 \cos \beta} + \frac{q_s \cos \beta}{r^2 \sin^2 \beta} - \left(\frac{\varepsilon}{Bo} \right) \frac{K^2 q_s^{2/3} \cos \beta}{3 r^{8/3} \sin \beta} \right] \\
& + \varepsilon^2 \left[-\frac{312482 K R e^2 q_s^{10/3}}{40425 r^{16/3} \sin^3 \beta} - \frac{136 K R e q_s^{7/3}}{315 r^{13/3} \sin \beta \cos \beta} + \frac{304 K R e q_s^{7/3} \cos \beta}{105 r^{13/3} \sin^3 \beta} \right. \\
& - \frac{2 K q_s^{4/3} \sin \beta}{3 r^{10/3} \cos^2 \beta} - \frac{451 K q_s^{4/3}}{72 r^{10/3} \sin \beta} + \frac{157 K q_s^{4/3} \cos^2 \beta}{120 r^{10/3} \sin^3 \beta} - \frac{21 K q_s^{4/3}}{40 r^{10/3} \sin^3 \beta} \\
& \left. + \left(\frac{\varepsilon}{Bo} \right) \left(\frac{32 R e q_s^2}{35 r^5 \sin^3 \beta} + \frac{34 q_s}{27 r^4 \sin \beta \cos \beta} + \frac{19 q_s \cos \beta}{3 r^4 \sin^3 \beta} \right) + \left(\frac{\varepsilon}{Bo} \right)^2 \frac{K^2 q_s^{2/3} \cos \beta}{9 r^{14/3} \sin^2 \beta} \right], \quad (B 12)
\end{aligned}$$

$$\begin{aligned}
S_2 = & \varepsilon \left(\frac{6 R e q_s^2}{5 r^2 \sin^2 \beta} + \frac{q_s}{r \cos \beta} \right) + \varepsilon^2 \left[\frac{169 K R e q_s^{7/3} \cos \beta}{140 r^{10/3} \sin^3 \beta} - \frac{K q_s^{4/3}}{6 r^{7/3} \sin \beta} + \frac{K q_s^{4/3} \sin \beta}{3 r^{7/3} \cos^2 \beta} \right. \\
& \left. - \frac{734 K R e^2 q_s^{10/3}}{525 r^{13/3} \sin^3 \beta} - \frac{206 K R e q_s^{7/3}}{105 r^{10/3} \sin \beta \cos \beta} + \left(\frac{\varepsilon}{Bo} \right) \left(\frac{q_s}{r^3 \sin \beta \cos \beta} - \frac{q_s \cos \beta}{r^3 \sin^3 \beta} \right) \right], \quad (B 13)
\end{aligned}$$

$$S_3 = \varepsilon^2 \left[\frac{12 K R e^2 q_s^{10/3}}{7 r^{10/3} \sin^3 \beta} + \frac{10 K R e q_s^{7/3}}{7 r^{7/3} \sin \beta \cos \beta} + \frac{3 K q_s^{4/3}}{r^{4/3} \sin \beta} - \left(\frac{\varepsilon}{Bo} \right) \frac{q_s}{r^2 \sin \beta \cos \beta} \right], \quad (B 14)$$

and

$$S_4 = -\varepsilon^2 \left(\frac{\varepsilon}{Bo} \right) \frac{q_s}{r \sin \beta \cos \beta}. \quad (B 15)$$

In Eq. (3.13), the functions $f_i(r)$ ($i = 0, 1$, and 2) can be expressed in the form

$$f_i(r) = \operatorname{Re}(f_i) + \operatorname{Im}(f_i) \mathbf{j}, \quad (B 16)$$

with

$$\operatorname{Re}(f_0) = -\frac{1}{3} \ln r, \quad \operatorname{Im}(f_0) = -\frac{K \omega r^{5/3} \sin \beta}{5 q_s^{2/3}}, \quad (B 17)$$

$$\begin{aligned}
\operatorname{Re}(f_1) = & \omega^2 \left(-\frac{2 R e r}{15 \cos \beta} - \frac{r^2 \tan^2 \beta}{18 q_s} \right) \\
& - \frac{4 K R e q_s^{4/3}}{7 r^{7/3} \sin \beta} + \frac{2 K q_s^{1/3}}{9 r^{4/3} \cot \beta} + \frac{2 K q_s^{1/3}}{3 r^{4/3} \tan \beta} - \left(\frac{\varepsilon}{Bo} \right) \frac{1}{3 r^2 \sin \beta}, \quad (B 18)
\end{aligned}$$

$$\operatorname{Im}(f_1) = \omega \left[-\frac{16 K^2 R e q_s^{2/3}}{105 r^{2/3}} - \frac{K^2 r^{1/3} \sin^2 \beta}{9 q_s^{1/3} \cos \beta} + \frac{K^2 r^{1/3} \cos \beta}{3 q_s^{1/3}} - \left(\frac{\varepsilon}{Bo} \right) \frac{K}{3 q_s^{2/3} r^{1/3}} \right], \quad (B 19)$$

and

$$\begin{aligned}
\operatorname{Re}(f_2) = & -\left(\frac{\varepsilon}{Bo}\right) \frac{K^2 \omega^4 r^{10/3} \sin \beta}{270 q_s^{7/3} \cot^2 \beta} + \omega^2 \left[-\frac{242 K R e^2 q_s^{4/3}}{3150 r^{4/3} \sin(2\beta)} - \frac{32 K R e \sqrt[3]{q_s} \sin \beta}{105 \sqrt[3]{r} \cos^2 \beta} \right. \\
& + \frac{K R e \sqrt[3]{q_s}}{420 \sqrt[3]{r} \sin \beta} - \frac{5 K r^{2/3}}{54 q_s^{2/3} \cot^3 \beta} - \frac{11 K r^{2/3}}{36 q_s^{2/3} \cot \beta} + \left(\frac{\varepsilon}{Bo}\right) \left(-\frac{4 R e}{15 r \sin(2\beta)} \right. \\
& \left. + \frac{13 \ln r \sin \beta}{81 q_s \cos^2 \beta} + \frac{\ln r}{9 q_s \sin \beta} \right) \left. - \frac{26248 K^2 R e^2 q_s^{8/3}}{40425 r^{14/3} \sin^2 \beta} - \frac{152 K^2 R e q_s^{5/3}}{315 r^{11/3} \cos \beta} \right. \\
& \left. - \frac{169 K^2 R e q_s^{5/3} \cos \beta}{210 r^{11/3} \sin^2 \beta} + \frac{19 K^2 q_s^{2/3}}{81 r^{8/3} \cot^2 \beta} + \frac{571 K^2 q_s^{2/3}}{216 r^{8/3}} + \frac{163 K^2 q_s^{2/3}}{360 r^{8/3} \tan^2 \beta} \right. \\
& \left. + \frac{7 K^2 q_s^{2/3}}{40 r^{8/3} \sin^2 \beta} - \left(\frac{\varepsilon}{Bo}\right) \left(\frac{8 K R e q_s^{4/3}}{21 r^{13/3} \sin^2 \beta} + \frac{74 K \sqrt[3]{q_s}}{81 r^{10/3} \cos \beta} + \frac{16 K \sqrt[3]{q_s} \cos \beta}{9 r^{10/3} \sin^2 \beta} \right) \right. \\
& \left. + \left(\frac{\varepsilon}{Bo}\right)^2 \frac{1}{6 r^4 \sin^2 \beta} \right], \tag{B 20}
\end{aligned}$$

$$\begin{aligned}
\operatorname{Im}(f_2) = & \omega^3 \left[\frac{44 K^2 R e^2 q_s^{2/3} \sqrt[3]{r}}{525 \cos \beta} - \frac{K^2 R e r^{4/3}}{210 \sqrt[3]{q_s} \cot^2 \beta} - \frac{2 K^2 r^{7/3} \sin^4 \beta}{189 q_s^{4/3} \cos^3 \beta} + \frac{K^2 r^{7/3} \sin^2 \beta}{21 q_s^{4/3} \cos \beta} \right. \\
& - \left(\frac{\varepsilon}{Bo}\right) \frac{11 K r^{5/3} \tan^2 \beta}{135 q_s^{5/3}} \left. + \omega \left[-\frac{8606 R e^2 q_s^2}{24255 r^3 \sin^2 \beta \cos \beta} + \frac{152 R e q_s}{315 r^2 \cos^2 \beta} + \frac{4 R e q_s}{35 r^2 \sin^2 \beta} \right. \right. \\
& - \frac{13 \sin^2 \beta}{27 r \cos^3 \beta} - \frac{145}{72 r \cos \beta} + \frac{13 \cos \beta}{40 r \sin^2 \beta} - \frac{7}{40 r \sin^2 \beta \cos \beta} \\
& \left. - \left(\frac{\varepsilon}{Bo}\right) \left(\frac{71 K^2 R e q_s^{2/3}}{630 r^{8/3} \sin \beta} + \frac{26 K^2 \tan \beta}{81 \sqrt[3]{q_s} r^{5/3}} + \frac{17 K^2 \cot \beta}{45 \sqrt[3]{q_s} r^{5/3}} \right) + \left(\frac{\varepsilon}{Bo}\right)^2 \frac{2 K}{63 q_s^{2/3} r^{7/3} \sin \beta} \right]. \tag{B 21}
\end{aligned}$$

REFERENCES

AKTERSHEV, S. P. 2010 Heat transfer in falling laminar-wavy liquid films. *Thermophys. Aeromech.* **17**, 359–370.

AKTERSHEV, S. P., ALEKSEENKO, V. S. & TSVELODUB, O. Yu. 2022 Theoretical modeling of fluid dynamics and heat transfer in wavy liquid films under complex flow conditions. *Thermophys. Aeromech.* **29** (1), 1–34.

ALEKSEENKO, S. V., NAKORYAKOV, V. E. & POKUSAEV, B. G. 1985 Wave formation on vertical falling liquid films. *Int. J. Multiph. Flow* **11** (5), 607–627.

ANISZEWSKI, W., SAADE, Y., ZALESKI, S. & POPINET, S. 2020 Planar jet stripping of liquid coatings: Numerical studies. *Int. J. Multiph. Flow* **132**.

BANDI, P., MODIGELL, M., GROB, S., REUSKEN, A., ZHANG, L., HENG, Y., MARQUARDT, W. & MHAMDI, A. 2018 On reduced modeling of mass transport in wavy falling films. *AIChE J.* **64** (6), 2265–2276.

BARREIRO-VILLAVERDE, D., GOSSET, A., LEMA, M. & MENDEZ, M. A. 2024 On the coupling instability of a gas jet impinging on a liquid film. *J. Fluid Mech.* **992**.

BENILOV, E. S. & ZUBKOV, V. S. 2008 On the drag-out problem in liquid film theory. *J. Fluid Mech.* **617**, 283–299.

BENJAMIN, T. B. 1957 Wave formation in laminar flow down an inclined plane. *J. Fluid Mech.* **2** (6), 554–573.

BENNEY, D. J. 1966 Long waves on liquid films. *J. Math. Phys.* **45** (2), 150–155.

BERTOLOTTI, F. P. 1997 Response of the blasius boundary layer to free-stream vorticity. *Phys. Fluids* **9** (8), 2286–2299.

BOGACKI, P. & SHAMPINE, L.F. 1989 A 3(2) pair of Runge-Kutta formulas. *Appl. Math. Lett.* **2** (4), 321–325.

CAMPOREALE, C. & RIDOLFI, L. 2012 Hydrodynamic-driven stability analysis of morphological patterns on stalactites and implications for cave paleoflow reconstructions. *Phys. Rev. Lett.* **108**, 238501.

CHAKRABORTY, S., NGUYEN, P.-K., RUYER-QUIL, C. & BONTOZOGLOU, V. 2014 Extreme solitary waves on falling liquid films. *J. Fluid Mech.* **745**, 564–591.

CHANG, H.-C. 1994 Wave evolution on a falling film. *Annu. Rev. Fluid Mech.* **26**, 103–136.

CHANG, H.-C. & DEMEKHIN, E. A. 2002 *Complex wave dynamics on thin films*. Elsevier.

CHANG, H.-C., DEMEKHIN, E. A. & KOPELEVICH, D. I. 1993a Construction of stationary waves on a falling film. *Comput. Mech.* **11** (5), 313–322.

CHANG, H.-C., DEMEKHIN, E. A. & KOPELEVICH, D. I. 1993b Nonlinear evolution of waves on a vertically falling film. *J. Fluid Mech.* **250**, 433–480.

CHAROGIANNIS, A. & MARKIDES, C. N. 2019 Spatiotemporally resolved heat transfer measurements in falling liquid-films by simultaneous application of planar laser-induced fluorescence (PLIF), particle tracking velocimetry (PTV) and infrared (IR) thermography. *Exp. Therm. Fluid Sci.* **107**, 169–191.

CRASTER, R. V. & MATAR, O. K. 2009 Dynamics and stability of thin liquid films. *Rev. Mod. Phys.* **81**, 1131–1198.

DAI, Z., ZHANG, Y., WANG, S., NAWAZ, K. & JACOBI, A. 2022 Falling-film heat exchangers used in desalination systems: A review. *Int. J. Heat Mass Transf.* **185**.

DENNER, F., CHAROGIANNIS, A., PRADAS, M., MARKIDES, C. N., VAN WACHEM, B. G. M. & KALLIADASIS, S. 2018 Solitary waves on falling liquid films in the inertia-dominated regime. *J. Fluid Mech.* **837**, 491–519.

DENNER, F., PRADAS, M., CHAROGIANNIS, A., MARKIDES, C. N., VAN WACHEM, B. G. M. & KALLIADASIS, S. 2016 Self-similarity of solitary waves on inertia-dominated falling liquid films. *Phys. Rev. E* **93** (3), 033121.

DIETZE, G. F. 2019 Effect of wall corrugations on scalar transfer to a wavy falling liquid film. *J. Fluid Mech.* **859**, 1098–1128.

DIETZE, G. F. 2024 Liquid plugs in narrow tubes: application to airway occlusion. *J. Fluid Mech.* **998**.

DIETZE, G. F., AL-SIBAI, F. & KNEER, R. 2009 Experimental study of flow separation in laminar falling liquid films. *J. Fluid Mech.* **637**, 73–104.

DIETZE, G. F., LAVALLE, G. & RUYER-QUIL, C. 2020 Falling liquid films in narrow tubes: occlusion scenarios. *J. Fluid Mech.* **894**.

DIETZE, G. F., ROHLFS, W., NÄHRICH, K., KNEER, R. & SCHEID, B. 2014 Three-dimensional flow structures in laminar falling liquid films. *J. Fluid Mech.* **743**, 75–123.

DURUK, S., SHEPHERD, R. G., BOUJO, E. & SELLIER, M. 2023 Three-dimensional nonlinear dynamics of a thin liquid film on a spinning ellipsoid. *Phys. Fluids* **35** (7).

GAO, D., MORLEY, N. B. & DHIR, V. 2003 Numerical simulation of wavy falling film flow using VOF method. *J. Comput. Phys.* **192** (2), 624–642.

GOVINDARAJAN, R. & NARASIMHA, R. 1995 Stability of spatially developing boundary layers in pressure gradients. *J. Fluid Mech.* **300**, 117–147.

GOVINDARAJAN, R. & NARASIMHA, R. 1997 A low-order theory for stability of non-parallel boundary layer flows. *Proc. Roy. Soc. Lond. A.* **453** (1967), 2537–2549.

HERBERT, T. 1997 Parabolized stability equations. *Annu. Rev. Fluid Mech.* **29** (1), 245–283.

HU, J., YANG, X., YU, J. & DAI, G. 2014 Numerical simulation of carbon dioxide (CO₂) absorption and interfacial mass transfer across vertically wavy falling film. *Chem. Eng. Sci.* **116**, 243–253.

JOO, S. W., DAVIS, S. H. & BANKOFF, S. G. 1991 Long-wave instabilities of heated falling films: two-dimensional theory of uniform layers. *J. Fluid Mech.* **230**, 117–146.

KALLIADASIS, S., RUYER-QUIL, C., SCHEID, B. & VELARDE, M. G. 2012 *Falling liquid films*. Springer.

KAPITZA, P. L. 1948 Wave flow of thin layers of a viscous fluid: I. Free flow. II. Fluid flow in the presence of continuous gas flow and heat transfer. In *Collected Papers of P. L. Kapitza* (ed. D. T. Haar), pp. 662–689. Pergamon, original paper: *Zh. Eksp. Teor. Fiz.* **18**, 3–28 (in Russian).

KAPITZA, P. L. & KAPITZA, S. P. 1949 Wave flow of thin layers of a viscous fluid. III. Experimental study of the wave flow regime. In *Collected Papers of P. L. Kapitza* (ed. D. T. Haar), pp. 690–709. Pergamon, original paper: *Zh. Eksp. Teor. Fiz.* **19**, 105–120 (in Russian).

KIM, D. J. & KIM, D. 2024 Low-order modelling of three-dimensional surface waves in liquid film flow on a rotating disk. *J. Fluid Mech.* **985**, A4.

KOFMAN, N., MERGUI, S. & RUYER-QUIL, C. 2014 Three-dimensional instabilities of quasi-solitary waves in a falling liquid film. *J. Fluid Mech.* **757**, 854–887.

LACANETTE, D., GOSSET, A., VINCENT, S., BUCHLIN, J. M. & ARQUIS, E. 2006 Macroscopic analysis of gas-jet wiping: Numerical simulation and experimental approach. *Phys. Fluids* **18** (4).

LEDDA, P. G., BALESTRA, G., LERISSON, G., SCHEID, B., WYART, M. & GALLAIRE, F. 2021 Hydrodynamic-driven morphogenesis of karst draperies: spatio-temporal analysis of the two-dimensional impulse response. *J. Fluid Mech.* **910**, A53.

LEDDA, P. G., PEZZULLA, M., JAMBON-PUILLET, E., BRUN, P.-T. & GALLAIRE, F. 2022 Gravity-driven coatings on curved substrates: a differential geometry approach. *J. Fluid Mech.* **949**, A38.

LIU, J. & GOLLUB, J. P. 1994 Solitary wave dynamics of film flows. *Phys. Fluids* **6** (5), 1702–1712.

LIU, J., PAUL, J. D. & GOLLUB, J. P. 1993 Measurements of the primary instabilities of film flows. *J. Fluid Mech.* **250**, 69–101.

MAKARYTCHEV, S. V., LANGRISH, T. A. G. & PRINCE, R. G. H. 2001 Thickness and velocity of wavy liquid films on rotating conical surfaces. *Chem. Eng. Sci.* **56** (1), 77–87.

MALAMATARIS, N. A., VLACHOGIANNIS, M. & BONTOZOGLOU, V. 2002 Solitary waves on inclined films: Flow structure and binary interactions. *Phys. Fluids* **14** (3), 1082–1094.

MENDEZ, M. A., GOSSET, A., SCHEID, B., BALABANE, M. & BUCHLIN, J. M. 2021 Dynamics of the jet wiping process via integral models. *J. Fluid Mech.* **911**.

MEURER, A., SMITH, C. P., PAPROCKI, M., ČERTÍK, O., KIRPICHEV, S. B., ROCKLIN, M., KUMAR, A., IVANOV, S., MOORE, J. K., SINGH, S., RATHNAYAKE, T., VIG, S., GRANGER, B. E., MULLER, R. P., BONAZZI, F., GUPTA, H., VATS, S., JOHANSSON, F., PEDREGOSA, F., CURRY, M. J., TERREL, A. R., ROUČKA, Š., SABOO, A., FERNANDO, I., KULAL, S., CIMRMAN, R. & SCOPATZ, A. 2017 SymPy: symbolic computing in Python. *PeerJ Comput. Sci.* **3**, e103.

MEZA, C. E. & BALAKOTAIAH, V. 2008 Modeling and experimental studies of large amplitude waves on vertically falling films. *Chem. Eng. Sci.* **63** (19), 4704–4734.

MIYARA, A. 1999 Numerical analysis on flow dynamics and heat transfer of falling liquid films with interfacial waves. *Heat Mass Transf.* **35** (4), 298–306.

MIYARA, A. 2000a Numerical analysis on heat transfer enhancement by waves on falling liquid film. *J. Therm. Sci.* **9**, 236–242.

MIYARA, A. 2000b Numerical simulation of wavy liquid film flowing down on a vertical wall and an inclined wall. *Int. J. Therm. Sci.* **39** (9–11), 1015–1027.

MOLEFE, L., ZAMPOGNA, G. A., KOLINSKI, J. M. & GALLAIRE, F. 2024 Coating thickness prediction for a viscous film on a rough plate. *J. Fluid Mech.* **1001**.

MUDUNURI, R. R. & BALAKOTAIAH, V. 2006 Solitary waves on thin falling films in the very low forcing frequency limit. *AIChe J.* **52** (12), 3995–4003.

NGUYEN, L. T. & BALAKOTAIAH, V. 2000 Modeling and experimental studies of wave evolution on free falling viscous films. *Phys. Fluids* **12** (9), 2236–2256.

NOSOKO, T., YOSHIMURA, P. N., NAGATA, T. & OYAKAWA, K. 1996 Characteristics of two-dimensional waves on a falling liquid film. *Chem. Eng. Sci.* **51** (5), 725–732.

NUSSELT, W. 1916 Die oberflächenkondensation des wasserdampfes. *VDI-Zs* **60**, 541.

PEREIRA, A. & KALLIADASIS, S. 2008 Dynamics of a falling film with solutal Marangoni effect. *Phys. Rev. E* **78**, 036312.

PINO, F., MENDEZ, M. A. & SCHEID, B. 2024 Linear stability analysis of a vertical liquid film over a moving substrate. *J. Fluid Mech.* **1000**.

PUGLISI, C., RISTIC, R., SAINT, J. & WILKINSON, K. 2022 Evaluation of spinning cone column distillation as a strategy for remediation of smoke taint in juice and wine. *Molecules* **27** (22), 8096.

QUÉRÉ, D. 1999 Fluid coating on a fiber. *Annu. Rev. Fluid Mech.* **31**, 347–384.

RAMASWAMY, B., CHIPPADA, S. & JOO, S. W. 1996 A full-scale numerical study of interfacial instabilities in thin-film flows. *J. Fluid Mech.* **325**, 163–194.

ROHLFS, W., PISCHKE, P. & SCHEID, B. 2017 Hydrodynamic waves in films flowing under an inclined plane. *Phys. Rev. Fluids* **2** (4), 044003.

ROHLFS, W. & SCHEID, B. 2015 Phase diagram for the onset of circulating waves and flow reversal in inclined falling films. *J. Fluid Mech.* **763**, 322–351.

RYER-QUIL, C. & MANNEVILLE, P. 2000 Improved modeling of flows down inclined planes. *Eur. Phys. J. B* **15**, 357–369.

RUYSER-QUIL, C., TREVELEYAN, P., GIORGIUTTI-DAUPHINÉ, F., DUPRAT, C. & KALLIADASIS, S. 2008 Modelling film flows down a fibre. *J. Fluid Mech.* **603**, 431–462.

SALAMON, T. R., ARMSTRONG, R. C. & BROWN, R. A. 1994 Traveling waves on vertical films: Numerical analysis using the finite element method. *Phys. Fluids* **6** (6), 2202–2220.

SAMANTA, A. 2023 An elliptic velocity profile-based two-equation model in viscous film. *Phys. Fluids* **35** (2).

SCHEID, B., RUYER-QUIL, C. & MANNEVILLE, P. 2006 Wave patterns in film flows: modelling and three-dimensional waves. *J. Fluid Mech.* **562**, 183–222.

SHEPHERD, R. G., BOUJO, E. & SELLIER, M. 2024 A general model for spin coating on a non-axisymmetric curved substrate. *J. Fluid Mech.* **998**, A32.

SHORT, M. B., BAYGENTS, J. C., BECK, J. W., STONE, D. A., TOOMEY, R. S. & GOLDSTEIN, R. E. 2005 Stalactite growth as a free-boundary problem: A geometric law and its platonic ideal. *Phys. Rev. Lett.* **94**, 018501.

SISOEV, G. M., MATAR, O. K. & LAWRENCE, C. J. 2005 Absorption of gas into a wavy falling film. *Chem. Eng. Sci.* **60** (3), 827–838.

STAFFORD, J., UZO, N., PICCOLI, E., PETIT, C. & MATAR, O. K. 2025 Thin film flow over a spinning disk: Experiments and direct numerical simulations. *Phys. Rev. Fluids* **10** (2), 024805.

TANGUY, G., DOLIVET, A., GARNIER-LAMBOUIN, F., MÉJEAN, S., COFFEY, D., BIRKS, T., JEANTET, R. & SCHUCK, P. 2015 Concentration of dairy products using a thin film spinning cone evaporator. *J. Food Eng.* **166**, 356–363.

VALLURI, P., MATAR, O. K., HEWITT, G. F. & MENDES, M. A. 2005 Thin film flow over structured packings at moderate Reynolds numbers. *Chem. Eng. Sci.* **60** (7), 1965–1975.

WEINSTEIN, S. J. & RUSCHAK, K. J. 2004 Coating flows. *Annu. Rev. Fluid Mech.* **36**, 29–53.

YIH, C.-S. 1963 Stability of liquid flow down an inclined plane. *Phys. Fluids* **6** (3), 321–334.

ZHOU, G. & PROSPERETTI, A. 2020a Capillary waves on a falling film. *Phys. Rev. Fluids* **5**, 114005.

ZHOU, G. & PROSPERETTI, A. 2020b A numerical study of mass transfer from laminar liquid films. *J. Fluid Mech.* **902**, A10.

ZHOU, G. & PROSPERETTI, A. 2022 Hydraulic jump on the surface of a cone. *J. Fluid Mech.* **951**, A20.

ZOLLARS, R. L. 1974 Linear hydrodynamic stability theory for thin film flow down cones and cylinders. PhD thesis, University of Colorado Boulder.

ZOLLARS, R. L. & KRANTZ, W. B. 1976 Laminar-film flow down a right circular cone. *Ind. Eng. Chem. Fundam.* **15** (2), 91–94.

ZOLLARS, R. L. & KRANTZ, W. B. 1980 Non-parallel flow effects on the stability of film flow down a right circular cone. *J. Fluid Mech.* **96**, 585–601.